Geochimica et Cosmochimica Acta 353 (2023) 158–170

Contents lists available at ScienceDirect

Geochimica et Cosmochimica Acta

journal homepage: www.elsevier.com/locate/gca

Sulfidation of Ni-bearing goethites to pyrite: The effects of Ni and implications for its migration between iron phases

Zhongkuan Wu [a], Tingting Zhang [a], Bruno Lanson [b], Hui Yin [c], Dong Cheng [a], Peng Liu [d], Feng He [a,e,*]

[a] College of Environment, Zhejiang University of Technology, Hangzhou 310014, China
[b] Univ. Grenoble Alpes, Univ. Savoie Mont Blanc, CNRS, IRD, Univ. Gustave Eiffel, ISTerre, F-38000 Grenoble, France
[c] Key Laboratory of Arable Land Conservation (Middle and Lower Reaches of Yangtse River), Ministry of Agriculture and Rural Affairs, College of Resources and Environment, Huazhong Agricultural University, Wuhan 430070, China
[d] School of Environmental Studies & State Key Laboratory of Biogeology and Environmental Geology, China University of Geosciences, Wuhan 430074, China
[e] Institute of Environmental Processes and Pollution Control, and School of Environment and Civil Engineering, Jiangnan University, Wuxi 214122, China

ARTICLE INFO

Associate editor: Juan Liu

Keywords:
Nickel
Goethite
Sulfidation
Iron sulfides
Pyrite
Migration

ABSTRACT

Goethite and pyrite are common iron minerals in oxic or anoxic environments, respectively, both minerals being major reservoirs for Nickel, a bio-essential element. Mineral transformation between goethite and pyrite is frequent owing to the alternation of oxic and anoxic conditions in sulfate-rich environments. This mineral transformation has been amply studied, but the effect of Ni on this transformation and its fate along it remain poorly understood. Sulfidation of Ni-free and Ni-containing (through adsorption or isomorphic substitution) goethites was thus studied experimentally by reacting goethite with dissolved S(-II) (molar Fe:S≈1:1). X-ray diffraction and associated Rietveld refinement, thermogravimetric analysis, scanning/transmission electron microscopy, X-ray absorption spectroscopy, and wet chemistry were used to monitor mineralogical evolutions and unravel Ni association with reaction products. After 44 days of sulfidation, about half of initial goethite converted to iron sulfides: thermodynamically stable pyrite (67%–93%) with minor contents of mackinawite (2%–15%) and greigite (5%–25%). Although the overall content of iron sulfides formed was essentially independent of Ni presence, Ni hampered the conversion from metastable iron sulfides (i.e., mackinawite and greigite) to pyrite (67%–78% vs. 93%, in the presence and absence of Ni, respectively). Pyrite formation from metastable sulfide precursors yielded a uniform Ni distribution in newly formed pyrite, regardless of the initial Ni association with goethite. Although no Ni was released to solution during pyrite formation, Ni incorporation to pyrite results in an increased risk of release to the environment as iron sulfides will be oxidized when exposed to air and water in supergene environments, leading to highly acidic conditions favoring Ni solubility and mobility.

1. Introduction

Laterite (Deoliveira et al., 1992; Dublet et al., 2015; Dublet et al., 2012; Fan and Gerson, 2015; Landers and Gilkes, 2007; Landers et al., 2009) and sulfide deposits (Ikogou et al., 2017; Morin et al., 2017; Noël et al., 2015; Swanner et al., 2019) represent the two most important Ni reservoirs in terrestrial environments (Elias, 2002). In both settings, goethite and pyrite are the two main host minerals for Ni. For example, goethite may present Ni-enrichment up to several weight percents (Dublet et al., 2012; Eliopoulos and Economou-Eliopoulos, 2000; Ugwu and Sherman, 2019) and commonly accounts for ~60–75% of the Ni pool in laterites (Fan and Gerson, 2015; Landers et al., 2009; Manceau et al., 2000). Goethite sequesters Ni, and other transition metals, via surface adsorption (Nachtegaal and Spark, 2002; Ugwu et al., 2019; Xu et al., 2006) and isomorphic substitutions (Cornell, 1991; de Carvalho-E-Silva et al., 2002; Dublet et al., 2015; Landers and Gilkes, 2007; Manceau et al., 2000). Ni(II) adsorbed to goethite surface is commonly considered to readily desorb, whereas incorporation in goethite crystal structure (Ugwu et al., 2019) results in a more stable sequestration. Both adsorbed and structurally incorporated Ni modify goethite's physico-chemical properties, affecting its subsequent reactivity, including phase transformation. In particular, adsorbed Ni(II) was reported to compete

* Corresponding author at: College of Environment, Zhejiang University of Technology, Hangzhou 310014, China.
E-mail address: fenghe@zjut.edu.cn (F. He).

https://doi.org/10.1016/j.gca.2023.06.001
Received 11 November 2022; Accepted 1 June 2023
Available online 7 June 2023

with other adsorbents for goethite surface sites (Xu et al., 2006) and to delay goethite recrystallization (Frierdich et al., 2019). Ni(II)-for-Fe(III) substitutions also influence vibrational properties of surface hydroxyl groups (de Carvalho-E-Silva et al., 2002), surface charge, or solubility (Ugwu and Sherman, 2019) of goethite particles in particular owing to the difference in valence of Fe(III) and Ni(II) in goethite crystal structure (de Carvalho-E-Silva et al., 2002; Frierdich et al., 2019; Gasser et al., 1996; Ugwu and Sherman, 2019; Zachara et al., 2001).

Although goethite is the most common and the thermodynamically most stable iron (oxyhydr)oxide on Earth (Cornell and Schwertmann, 2004), it may be altered under reducing conditions through interactions with microorganisms (Maurice et al., 2000; Zachara et al., 2001), organic compounds (Gasser et al., 1996; Larsen and Postma, 2001; Suter et al., 1991), or inorganic reductants (Poulton et al., 2004; Rickard, 1974; Suter et al., 1991). As a result, goethite may be dissolved (Dos Santos Afonso and Stumm, 1992) or transformed to secondary Fe minerals such as iron sulfides (e.g. pyrite, mackinawite, etc.) as the result of its interaction with dissolved sulfides [including H_2S, HS^-, and S(-II), hereafter globally referred to as S(-II)] (Poulton et al., 2004; Rickard, 1974; Wan et al., 2017; Wang and Morse, 1996). Such reducing conditions are commonly found in flooded sulfate-rich farmlands, wetlands, and marshes, where S(-II) could accumulate up to ~15 mM as the result of microbial anaerobic respiration (Bagarinao, 1992). A wealth of literature has been devoted to deciphering the interaction of goethite and other iron (oxyhydr)oxides with S(-II), a process commonly referred to as sulfidation (Kumar et al., 2018; Poulton et al., 2004; Rickard and Luther, 2007; Rickard, 1974; Wan et al., 2017), iron (oxyhydr)oxides being regarded as the main iron suppliers for the early diagenetic formation of pyrite (Canfield, 1989). Goethite sulfidation is of particular importance as it is regarded as the starting point for sedimentary pyrite formation (Rickard, 1974), resulting in the association of goethite and pyrite under reducing (Seyfferth et al., 2020) or alternating oxidizing and reducing conditions (Otero et al., 2009). Mechanisms of goethite [or other iron (oxyhydr)oxides] sulfidation are well documented: first, S(-II) is adsorbed to the surface of the iron (oxyhydr)oxide allowing an electron-transfer from S(-II) to Fe(III) to form Fe(II), elemental sulfur (S^0), and polysulfides (S_n^{2-}) (Luther, 1991). S(-II) in excess then precipitates with Fe(II) to form amorphous FeS_x clusters, that transform first to crystalline but metastable monosulfides (mackinawite) and then to greigite. A final reaction between metastable iron sulfides (MIS: mackinawite and greigite) and S^0, S_n^{2-}, or H_2S produces thermodynamically stable pyrite (de Carvalho-E-Silva et al., 2002; Hurtgen et al., 1999; Lan and Butler, 2014; Luther, 1991; Pyzik and Sommer, 1981; Rickard and Luther, 2007; Schoonen and Barnes, 1991b; Wang and Morse, 1996).

In S(-II)-rich sediments, sulfidation of goethite and other Fe (oxyhydr)oxides is a typical process of reductive-dissolution and recrystallization (Luther, 1991; Wang and Morse, 1996), and as such strongly influences transport and bioavailability of foreign metals initially associated to goethite (Hockmann et al., 2020; Zachara et al., 2001). The sole reductive-dissolution of goethite and other iron (oxyhydr)oxides releases both adsorbed [like As and Ni – (Huang et al., 2015; Ren et al., 2018)] and substituted [like Al, Co, Mn, Ni, Cr – (Dubbin and Bullough, 2017; Landers and Gilkes, 2007; Maurice et al., 2000)] foreign elements to aquatic systems. In particular, structurally incorporated Ni(II) may be released to the aqueous phase during a bacteria mediated (Zachara et al., 2001) or HCl caused (Landers and Gilkes, 2007) reductive-dissolution of goethite, or lost during the lateritization process (Dublet et al., 2015). In contrast, when reductive-dissolution occurs in the presence of S(-II), an efficient reducing species (Canfield, 1989; Canfield et al., 1992), this species can readily coprecipitate with both Fe(II) and Ni(II) (Morse and Luther, 1999) thus leading to the formation of solid metal sulfides. Interestingly, the fate of Ni along goethite sulfidation and its effect on this process remain sparingly documented although iron sulfides are also important Ni sinks in sediments (Ikogou et al., 2017; Noël et al., 2015).

To bridge this knowledge gap, the present study investigated experimentally the sulfidation of goethite containing adsorbed or isomorphically substituted Ni, to decipher Ni transfer from oxic laterite deposits to anoxic sulfide deposits. Both the mineralogical transformations and Ni retention were characterized using X-ray diffraction, electron microscopy, thermogravimetric analysis, X-ray absorption spectroscopy, and wet chemistry. The main goal of the present work was to elucidate the fate of both adsorbed and substituted Ni(II) species during goethite sulfidation and Ni influence on the process.

2. Experimental methods

2.1. Goethite preparation

Ni-free goethite was prepared according to a modified version of Cornell and Schwertmann (2004) protocol. Briefly, 600 mL of a 0.167 M $Fe(NO_3)_3$ solution was prepared from the dissolution of $Fe(NO_3)_3{\cdot}9H_2O$ into MilliQ water (18.2 MΩ.cm) in a plastic beaker. Then, 180 mL of 5 M KOH was added in the above solution at a 5 mL/min rate with continuous stirring. The obtained suspension was then diluted to 2 L using MilliQ water, and let to settle down and age at room temperature for 7 days. The resulting precipitate was subsequently washed with 400 mL oxalate/ammonium oxalate solution (pH = 3) for 2 hrs to remove amorphous precipitates and adsorbed species, and dialyzed until conductivity was <20 μS/cm. The resulting paste was finally centrifuged, freeze-dried, ground, and sieved (100 mesh). Ni-incorporated goethites were synthesized along the same protocol but using mixed $Fe(NO_3)_3$ and $Ni(NO_3)_2$ solutions with Ni/(Ni + Fe) molar ratios of 0.02 or 0.06 (Ugwu and Sherman, 2019). Resulting samples are hereafter referred to as Gt, GtNi2, and GtNi6, according to the initial Ni contents.

Additional Ni-bearing goethite samples were obtained from sorption experiments: 150 mL of a 0.01 M (or 0.04 M) $Ni(NO_3)_2$ solution were added to 150 mL of a 10 g/L Gt suspension, the mixed solution being stirred for 24 hrs. Both Gt suspension and $Ni(NO_3)_2$ solution were prepared using a 0.01 M $NaNO_3$ ionic background. Before mixing, the suspension pH was adjusted to 6.00 and allowed to vary by less than ±0.05 pH units for 12 hrs. The final suspension was centrifuged and washed twice, before being freeze-dried. Resulting solids are hereafter referred to as GtANi5 (GtANi20).

The relative contents of Fe and Ni for Ni-containing goethites were determined by dissolving 10 mg of solids into 10.00 mL of 6 M HCl solution in duplicates, and metal concentration was measured via Atomic Absorption Spectroscopy (AAS). Results are shown in Table 1.

2.2. Sulfidation experiments

Goethite sulfidation experiments were performed in a glovebox [(Mikrouna, 100% Ar), maintained at < 1 ppm (v/v) O_2 using a copper catalyst] at room temperature (~23 °C) using a protocol similar to that of previous studies (Hockmann et al., 2020; Wan et al., 2017). Reagents and MilliQ water used in this part were purged with N_2 for more than 4 hrs before being transferred to the glovebox to minimize O_2 content of reacting solutions/suspensions prepared in the glovebox. 1.00 g of Gt, GtNi2, GtNi6, GtANi5, and GtANi20 were then added to 1 L of a 11.24 mmol Na_2S solution (Fe:S molar ratio ≈1), whose pH was adjusted to 6.00 ± 0.10 using HCl and maintained for 12 hrs before goethite addition. Each set was gently stirred with a magnetic stirrer for several mins

Table 1
Relative content of Ni and Fe in synthetic goethites.

Samples	c_{Fe} (mg/g)	c_{Ni} (mg/g)	Ni/(Fe + Ni) at.%
GtNi2	572.1 ± 3.3	6.66 ± 0.11	1.1
GtNi6	557.1 ± 1.7	13.26 ± 0.05	2.2
GtANi5	573.8 ± 3.5	6.56 ± 0.05	1.1
GtANi20	566.9 ± 3.4	9.12 ± 0.02	1.5

every day, and the pH was monitored and adjusted manually with HCl or NaOH as needed.

At certain time intervals, aliquots were withdrawn for analysis of aqueous and/or solid phases. Aqueous samples were filtered through 0.22 μm nylon membrane (the filtration may be repeated up to 8 times until the solution got colorless due to the formation of colloidal FeS at the beginning of the sulfidation) before further measurement. Ni concentration in solution was determined with AAS, that of Fe(II) with the phenanthroline method (Fadrus and Malý, 1975), and that of dissolved sulfides via the methylene blue method (Cline, 1969; Hockmann et al., 2020). Solid samples were retrieved by centrifugation and subsequently dried in the glovebox for several days. They are named as Sample_name-Reaction_time; for example, Gt-44d was obtained from Gt reacting with S(-II) for 44 days. Elemental sulfur (S^0) present on the surface of sulfidized solids was measured using a methanol extraction method: 7.0 mg of solids were added to 7.00 mL of methanol, the mixture being then sonicated for 10 mins, and S^0 content being then determined using high-performance liquid chromatography (Agilent-1260).

2.3. Characterization of goethites and of their sulfidized products

Mineralogy of Ni-free/-bearing goethites, and of their sulfidized counterparts was determined by X-ray diffraction (XRD), using a Bruker D8 Advance diffractometer equipped with a Cu Kα source (λ = 1.5418 Å, voltage 40 kV, current 40 mA), and using a scanning rate of 1°/min and 0.02° step size. Quantitative phase analysis of sulfidized samples was performed through the Rietveld refinement of XRD data using the Profex software (Döbelin, 2015; Döbelin and Kleeberg, 2015). Thermogravimetric analysis (TGA, Mettler) was performed from room temperature to 800 °C at a heating rate of 10 °C/min and under a continuous N_2 flow of 20 mL/min. Scanning electron microscopy (SEM) observations were performed on a Zeiss Sigma300 instrument operated with an accelerating voltage of 30 kV and a working distance of 50 mm. Transmission electron microscopy (TEM) investigations were performed on a FEI Tecnai G2 F30 microscope operated at 300 kV. STEM-HAADF (scanning transmission electron microscopy – high-angle annular dark field) images were obtained using Bruker Super Lite X2.

Fe K-edge extended X-ray absorption fine structure (EXAFS) spectra were recorded at the 4B9A beamline of the Beijing Synchrotron Radiation Facility (BSRF). A metallic Fe foil (E_0 = 7112 eV) was systematically used for energy calibration before data collection; data was collected at room temperature and in transmission mode over the 6920–7920 eV range. Data reduction was performed using Athena (Ravel and Newville, 2005). Fourier transform (FT) of k^3-weighted χ(k) data was performed over the 2.9–12.2 $Å^{-1}$ k-range to obtain the radial distribution function (RDF) χ(r) in real space.

2.4. Acid dissolution

From the literature, goethite (α-FeOOH), mackinawite [$(Fe,Ni)_{1+x}S$], and greigite [$Fe(II)Fe(III)_2S_4$] are readily soluble in (hot) HCl. Pyrite does not usually dissolve in HCl (Cooper and Morse, 1998; Cornwell and Morse, 1987; Morse et al., 1987), although nanocrystallinity may allow pyrite dissolution in HCl (Cooper and Morse, 1998; Cornwell and Morse, 1987; Morse et al., 1987), but is readily dissolved in HNO_3. A HCl-HNO_3 sequential treatment was thus modified from that of Huerta-Diaz and Morse (1990) to determine the association of Ni with iron oxides/sulfides according to their Fe/Ni release behavior. Specifically, 100 mg of sulfidized samples were added to 100 mL of 3 M HCl in a capped conical flask and kept at 40 °C using a water bath. Magnetic stirring could not be used owing to the highly magnetic character of sulfidized solids, and flasks were thus shaken for 5 mins to homogenize the solution every day and before each sampling. After 4 days in HCl, goethite, mackinawite, and greigite were supposed to be fully dissolved, with only pyrite being left. The residual solid was then filtered and washed twice, before being transferred in 45 mL of 2 M HNO_3. During both acid treatments, aliquots were sampled at different time intervals to determine Fe and Ni concentrations using AAS. After ~120 hrs of treatment in 2 M HNO_3, solids could still be observed, which could be dissolved completely by adding 10 mL of aqua regia.

3. Results

3.1. Powder X-ray diffraction

Synthesized Ni-free Gt yielded a diffraction pattern typical for goethite (Fig. 1, ICDD#29-0713). XRD patterns of Ni-bearing goethites were essentially similar to that of Gt, without additional diffraction lines, indicating Ni incorporation in goethite crystal structure or sorption at its surface. After reacting with S(-II) under anoxic conditions for 3 days, XRD patterns of reacted samples were similar to those of their unreacted counterparts, whereas modifications were visible from 7 days of reaction and on (Fig. S1). XRD patterns of Ni-free and Ni-bearing samples were dominated by peaks at ~21.2°/~36.6° (2θ – goethite 110 and 111 reflections – Fig. 1), whereas after sulfidation the peak at ~33.1° (2θ – pyrite 200 reflection) became most intense for all samples. Consistently, intensities of goethite peaks at ~53.3°, ~59.1°, ~61.4°, and ~64.0° (2θ – goethite 221, 151/160, 002, and 061 reflections, respectively) significantly decreased with increasing reaction time. In addition, peaks at ~36.6°, ~47.3°, ~59.1°, and ~61.4° (2θ) shifted to higher angles (green arrows in Fig. 1), and the peak at ~36.6° (2θ) was split on its high-angle side (blue arrow in Fig. 1). These evolutions indicated the formation of new phase(s) at the expense of goethite. Additional reflections at ~28.5° and ~56.3° (2θ) were attributed to pyrite (111 and 311 reflections, respectively - ICDD#42-1340), those at ~30.1°, ~39.0°, and ~49.6° (2θ) to mackinawite (101, 111, and 200 reflections, respectively - ICDD#15-0037), whereas weak peaks at ~25.4° and ~52.4° (2θ) indicated the presence of greigite (220 and 440 reflections, respectively - ICDD#16-0713) in reaction products, consistent with previous reports of goethite sulfidation (Wang and Morse, 1996). No nickel sulfides, other iron (oxyhydr)oxides, or S^0 were detected using XRD, although the latter was reported in similar studies (Hockmann et al., 2020; Rickard, 1974).

Quantitative phase analysis was performed using the Rietveld method to quantify the contributions of the four Fe-bearing minerals

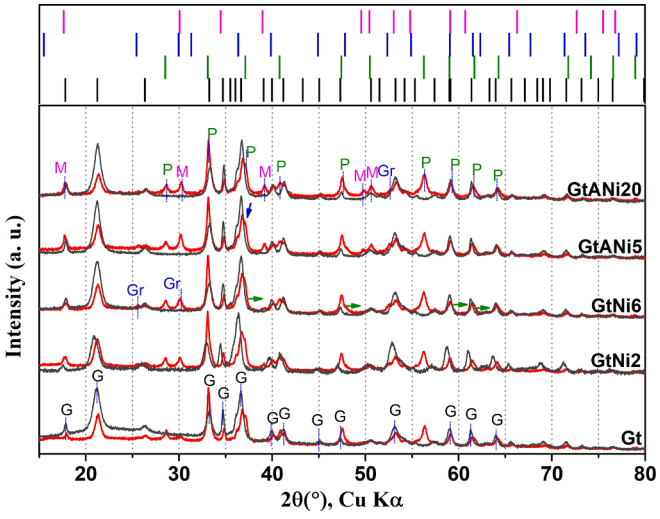

Fig. 1. Powder XRD patterns obtained from pristine Ni-free/-containing goethites (black) and from the corresponding reaction products after 44 days of interaction with S(-II) (red). G = goethite, P = pyrite, Gr = greigite, and M = mackinawite. Bars, from bottom to top, above these patterns are characteristic diffraction lines for: goethite (ICDD#29-0713; black), pyrite (ICDD#42–1340; green), greigite (ICDD#16–0713; blue), and mackinawite (ICDD#15-0037; magenta).

identified in sulfidized samples (Fig. 2, Table S1) in an effort to monitor sulfidation progress. Colloidal FeS and FeS_x clusters remain undetected by this approach however. After 3 days of reaction, minor amounts (~1–2%) of iron sulfide minerals were detected in all runs. After 7 days, ~40% of initial Gt and GtNi6 was converted to iron sulfides, mainly pyrite, that is more than that in GtANi5-7d and GtANi20-7d (~32%), possibly because the pre-existing sorption of Ni(II) to the goethite surface (Hellige et al., 2012; Hockmann et al., 2020; Wan et al., 2017) hindered the interaction of S(-II) with structural Fe(III) (Luther, 1991) during the early stages of GtANi5 and GtANi20 sulfidation, consistent with previous reports (Biber et al., 1994; Poulton et al., 2004). Goethite sulfidation then proceeded, with about half of initial goethite being transformed to sulfides after 44 days of reaction. For example, sulfide content was ~59% in Gt-44d (Table S1), a content significantly higher than that in sulfidized Ni-bearing goethites (~46–52%, Table S1), suggesting that the association of Ni incorporated in or adsorbed to goethite significantly hampered its conversion to iron sulfides. For all samples, pyrite was the main crystalline product of goethite sulfidation (~33%–54%) (Rickard, 1974), with a minor contribution of greigite (~3%–12%) and mackinawite (~1%–8%), the latter two being commonly considered as pyrite precursors (Luther, 1991; Rickard and Luther, 2007). Consistently, the overall content of metastable iron sulfides (MIS: mackinawite, greigite) remained limited in all reacted samples, suggesting that pyrite was formed at the expense of MIS or that MIS formation was inhibited. In addition, MIS appeared less abundant in Gt reaction products compared to Ni-bearing goethite reaction products.

Incorporation of Ni in goethite led to a minor distortion of its crystal framework, and more especially to a slight expansion of its b unit-cell parameter from 9.957(6) to 9.966(8) Å, a and c unit-cell parameters remaining essentially unchanged (Table S2), consistent with previous reports (Wells et al., 2006). By contrast, unit-cell parameters of the two Ni-adsorbed samples are logically almost identical to those of Gt. After 44 days of sulfidation, the low contents of greigite and mackinawite generate large uncertainties on their unit-cell parameters precluding an unambiguous assessment of their evolution. Unit-cell parameters of pyrite formed both from Ni-free and Ni-bearing goethites are identical within uncertainty.

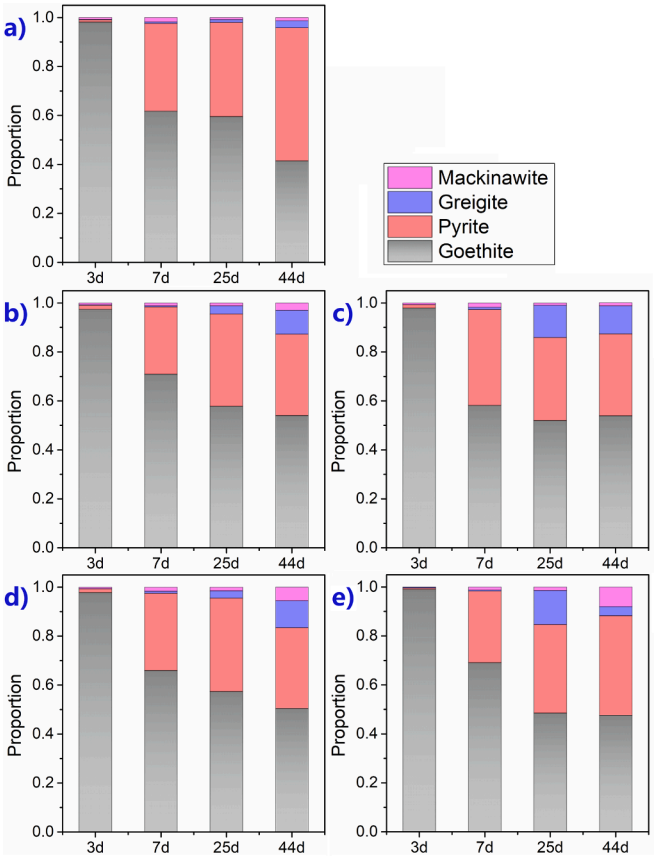

Fig. 2. Evolution as a function of reaction time of the mineralogy of reaction products of Ni-free/-containing goethites after their interaction with S(-II): a): Gt, b): GtNi2, c): GtNi6, d): GtANi5, and e): GtANi20. Errors on mineral fractions are given in Table S1.

3.2. *Evolution of Fe local environments*

Consistent with the above-described mineralogical evolution along goethite sulfidation, Fe local environment was modified as shown by the evolution of Fe K-edge EXAFS spectra (Fig. S2) and of corresponding

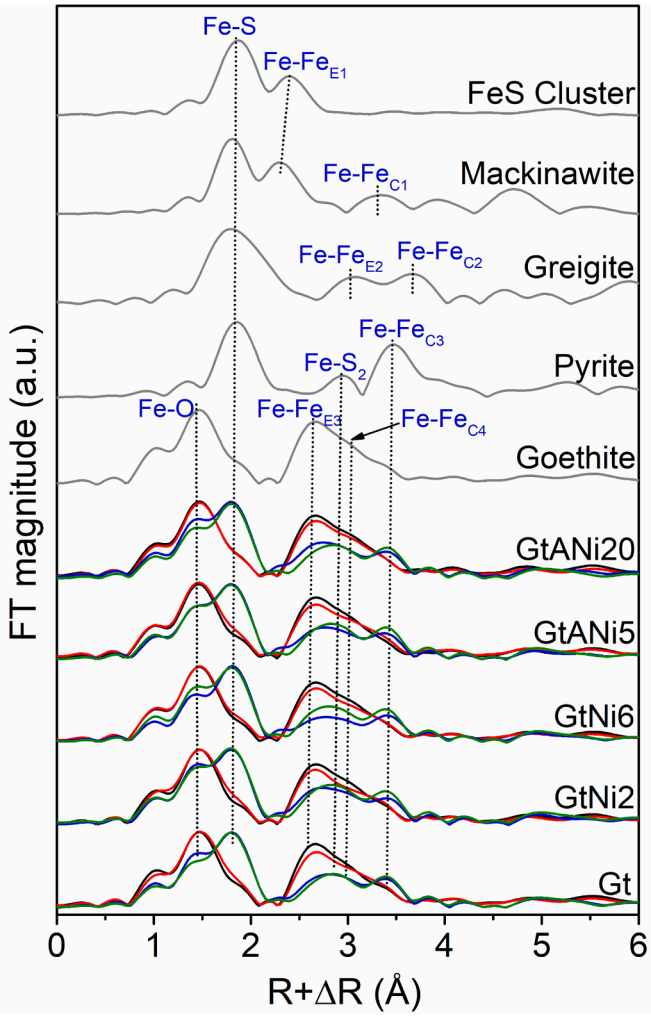

Fig. 3. Fourier transforms of Fe K-edge EXAFS spectra obtained for pristine (black) and sulfidized goethite samples (red: 3 days, blue: 7 days, green: 44 days), and iron oxhydroxide/sulfide standards (gray). To highlight the evolution of Fe local environment, FT intensities were normalized to that of the first shell. Data for colloidal FeS from Noël et al. (2020). Fourier transform for greigite was computed from the Fe K-edge EXAFS spectrum calculated with Feff8.4 based on greigite structure model (COD#9000123 – Ikogou et al., 2017). For mackinawite, Fe-Fe_{E1} and Fe-Fe_{C1} indicate edge- and corner-sharing linkages of FeS_4-FeS_4 tetrahedra; for greigite, Fe-Fe_{E2} and Fe-Fe_{C2} indicate edge- and corner-sharing linkages between FeS_6-FeS_6 octahedra and FeS_4/FeS_6-FeS_6 polyhedra, respectively; for pyrite, Fe-S_2 and Fe-Fe_{C3} indicate the second nearest Fe-S shell and corner-sharing linkages of FeS_6 octahedra, respectively; for goethite, Fe-Fe_{E3} and Fe-Fe_{C4} indicate edge- and corner-sharing linkages of FeO_6-FeO_6 octahedra, respectively.

RDFs (Fig. 3). It was not possible to determine relative proportions of the different Fe-bearing phases from linear combination fitting of the EXAFS spectra however. All attempts to fit EXAFS data using reference spectra of colloidal FeS (Noël et al., 2020), mackinawite, greigite, pyrite, and goethite did not allow reaching a satisfactory fit (not shown), thus precluding comparison with the mineralogy determined from Rietveld refinement of the XRD data (Table S1, Fig. S1). The inability to fit the EXAFS signature of the solid fraction is likely related to contrasting signatures of FeS_x clusters present in the solid fraction and of the colloidal FeS reference that was obtained from filtered (<0.02 μm) solutions by Noël et al. (2020) as suggested by the mismatch between the spectral signature of colloidal FeS and the modification of EXAFS spectra after 3 days of sulfidation (Figs. S2 and S3). In both k- and r-space, pristine samples data was typical of goethite (Burton et al., 2010; Hohmann et al., 2011), with a first maximum at ~1.50 Å (R + ΔR) in r-space corresponding to the first Fe-O shell and an asymmetric peak spanning from ~2.30 to ~3.60 Å (R + ΔR), peaking at ~2.70 Å (R + ΔR), and corresponding to Fe-Fe bonds in goethite edge- and corner-sharing FeO_6 octahedra. After reacting for 3 days with S(-II), the frequencies of goethite EXAFS spectra in k-space were essentially alike those of pristine samples. Amplitudes were attenuated however (Fig. S2), the modification being most significant for Gt relative to Ni-bearing goethites (Fig. S3), suggesting a negative effect of Ni on goethite sulfidation. Consistently, the Fe-Fe shell at ~2.70 Å (R + ΔR) in r-space decreased slightly (Fig. 3), supporting a minor decrease in the number of edge-sharing linkages between FeO_6 octahedra in goethite. In addition, the minor increase of the shoulder at ~1.80 Å (R + ΔR) (Fig. 3) supports the early formation of Fe–S bonds, consistent with the formation of FeS_x clusters. After 7–44 days of sulfidation, Fe K-edge spectra were strongly modified compared to that of pristine samples with a major evolution of frequencies in k-space (Figs. S2 and S3). Consistently, the main contribution to the first coordination shell of Fe shifted from ~1.50 Å to ~1.80 Å (R + ΔR); similarly, the asymmetric peak extending from ~2.30 to ~3.60 Å (R + ΔR) with a maximum at ~2.70 Å (R + ΔR) in pristine samples weakened and split into two isolated peaks of similar intensity at ~2.80 Å and ~3.40 Å (R + ΔR). The peak at ~2.80 Å combines the contributions from edge-sharing Fe-Fe linkages of FeO_6 octahedra in goethite and from Fe-S_{2nd} linkages in pyrite, whereas that at ~3.40 Å (R + ΔR) is related to the nearest Fe-Fe shell in pyrite (corner-sharing linkages of FeS_n polyhedra). These modifications are consistent with the conversion of a significant fraction of goethite to iron sulfides after 44 days of sulfidation, most of the conversion occurring from 3 to 7 days of sulfidation, consistent with XRD results (Figs. 1, 2, and S1, and Table S1). On the difference plots between reacted and initial samples (Fig. S3), reacted Gt samples systematically showed significantly stronger differences (both after 3 and 44 days of sulfidation), compared to GtNi6 and GtANi20 supporting the negative effect of Ni association to goethite on its sulfidation.

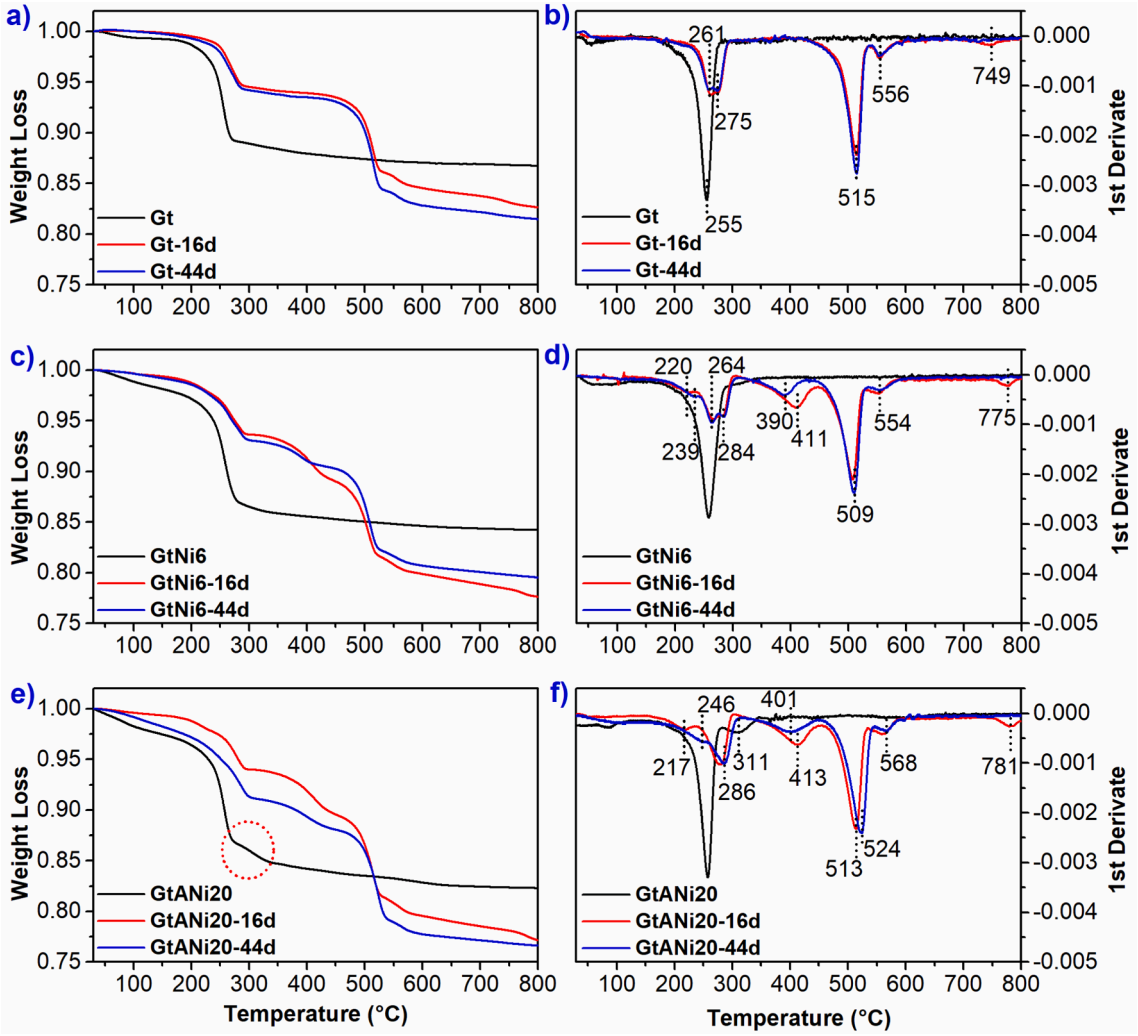

Fig. 4. Experimental thermogravimetric curves (left) and their first derivatives (right) for pristine (black) and sulfidized goethite samples (red: 16 days, blue: 44 days): a,b) Gt; c,d): GtNi6; e,f) GtANi20.

3.3. Thermogravimetric analysis

Consistent with the observed mineralogical evolution upon goethite sulfidation, the thermogravimetric analysis of unreacted and reacted samples differed significantly (Fig. 4). All goethite samples (with or without Ni) exhibited a significant weight loss from ~170 °C to ~300 °C with a maximum at ~255 °C typical for goethite dehydroxylation and conversion to hematite [α-Fe_2O_3 – (Cornell and Schwertmann, 2004; Ponomar, 2018)]. Weight losses occurring prior to dehydroxylation were ascribed to the loss of physisorbed water. An additional weight loss was observed at ~300 °C for GtANi20 (Fig. 4e), which is possibly related to the presence of adsorbed Ni(II) on goethite surface. Compared to pristine samples, goethite dehydroxylation weight loss was still observed in sulfidized samples, consistent with the presence of unreacted goethite, but shifted to slightly higher temperature (~270 °C) compared to unreacted samples. In addition, the splitting of TGA data first derivative observed over this low-temperature range (Fig. 4b,d) suggests the contribution of another process to the weight loss of sulfidized samples. The temperature shift of goethite dehydroxylation weight loss could correspond to a morphological/size evolution of unreacted goethite whereas the additional process possibly results from the partial conversion of greigite (Krs et al., 1993; Kyprianidou-Leodidou et al., 1997; Sagnotti and Winkler, 1999). For all sulfidized goethites, two major weight losses were observed at ~510–525 °C and ~555–570 °C (Fig. 4) that are typical for pyrite (Yang et al., 2019). Two additional weight losses were observed at low temperatures (~215/220 °C and ~240/245 °C) in sulfidized Ni-containing goethites. These weight losses are possibly related to the presence of Ni- or Ni-rich phases [possibly $Ni_{1-x}S$ – (Bishop et al., 1999)] as they were not observed for sulfidized Ni-free Gt and did not appear to be related to the presence of a specific Fe sulfide species. These Ni-rich phases were not detected using XRD however. Another weight loss was observed at 390/415 °C in the TGA curves of sulfidized Ni-bearing goethites (Fig. 4d,f), but was absent in the reacted Ni-free Gt (Gt-16d/44d). This weight loss is possibly ascribed to the decomposition of NiS_2 to NiS (Dunn and Kelly, 1977).

3.4. Electron microscopy

Goethite sulfidation and the associated crystallization of Fe-rich sulfides (pyrite, greigite, mackinawite) were associated with a dramatic morphological evolution (Fig. 5 and S4). All pristine goethite samples were acicular shaped with lath lengths ranging ~300–400 nm or more, typical for goethite (Cornell and Schwertmann, 2004), and no significant difference was detected between Gt and Ni-bearing samples. Crystal habits were more heterogeneous in sulfidized samples with three main crystal habits: i) laths extending ~100–300 nm in length and corresponding to residual goethite after their interaction with S(-II); ii) framboids extending several hundred nanometers in diameter and composed of cubic pyrite nanocrystals (Wang and Morse, 1996); iii) irregular lamellas, possibly corresponding to greigite as suggested by lattice fringes exhibiting ~0.350 and 0.285 nm periodicities [greigite (220) and (222) planes; Fig. S4f,i – (Cao et al., 2009; Islam and Patel, 2017; Lan and Butler, 2014)]. Although Rietveld refinement indicated that half of the initial goethite was preserved in sulfidized samples (Table S1), the framboids and irregular lamellas visually dominated the three sulfidized samples, suggesting that residual goethite might be covered by newly formed iron sulfides. Contrasting with micrometer-sized cubic/polyhedral pyrite crystals reported previously (Butler and Rickard, 2000; Du et al., 2021; Liu et al., 2022; Lowers et al., 2007), pyrite grain sizes ranged from tens to hundreds of nanometers in the present sulfidized goethites. Consistent with previous TEM observations (Kumar et al., 2018; Peiffer et al., 2015), no joints between pyrite framboids and goethite laths were observed, thus confirming that the goethite-to-iron sulfides transformation proceeded mainly through dissolution–recrystallization (Wang and Morse, 1996), rather than as a solid-state conversion.

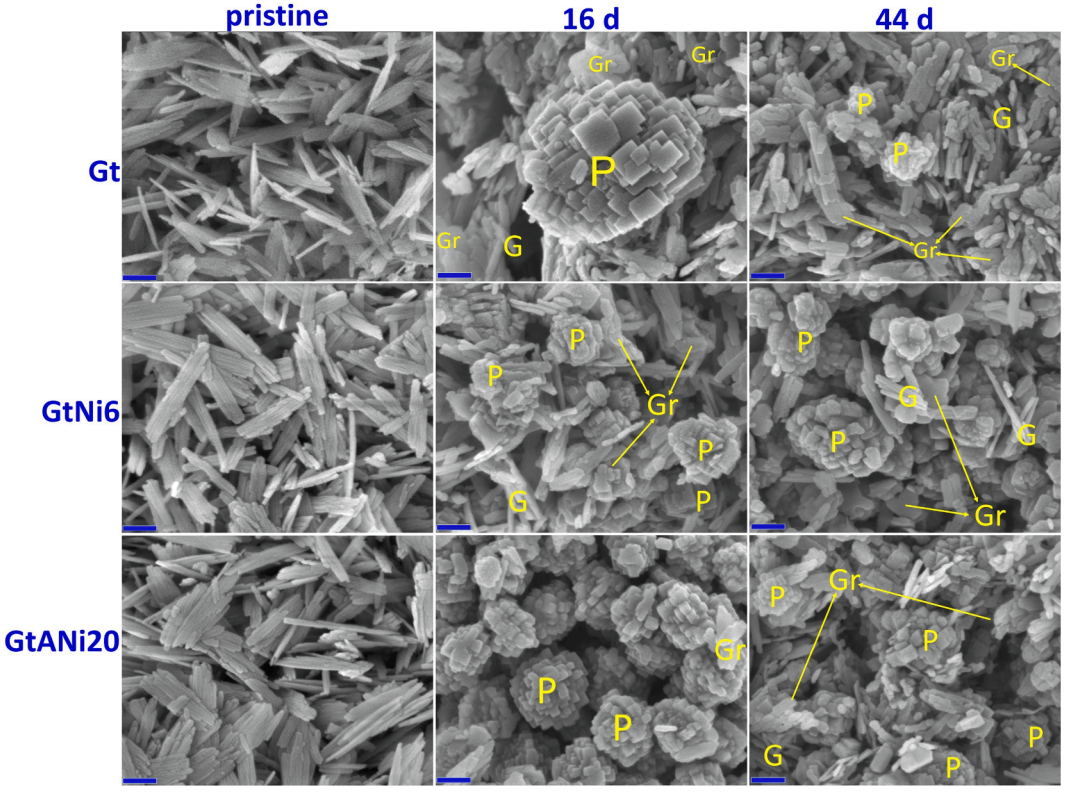

Fig. 5. Scanning electron micrographs of pristine and sulfidized Ni-free/-bearing goethites. G, P, Gr, and M stand for goethite, pyrite, greigite, and mackinawite, respectively. Blue scale bars at the lower left of each figure represent 100 nm.

3.5. Solution chemistry during sulfidation (S(-II) and Fe(II) concentrations)

S(-II) concentration in solution decreased dramatically below the detection limit of the methylene blue method (0.02 mg/L) within 3 days (Fig. 6a). S(-II) consumption rate was similar for all goethite samples. This decrease resulted from the quick adsorption of S(-II) to goethite surface and from the subsequent swift formation of amorphous FeS_x clusters induced by S(-II) interactions with Fe(II) (Poulton, 2003; Wan et al., 2017) according to:

$$2Fe(III)OOH + S(-II) \rightarrow 2Fe(II) + S^0 \quad (1)$$

$$Fe(II) + xS(-II) \rightarrow Fe(II)S_x \quad (2)$$

Consistently, Fe(II) and elemental sulfur (S^0) were produced as the result of these interactions immediately after adding goethite to the S(-II) solution (Fig. 6b,c). After an initial steady increase, Fe(II) content in solution stabilized after ~15 days of sulfidation, most likely because Fe(II) consumption related to Fe sulfides formation compensated its production according to Eq. (1), and to the subsequent destabilization of both FeS_x clusters/colloidal FeS and MIS. After a possible sharp initial increase (not detected), S^0 amount decreased gradually in the system most likely as the result of pyrite formation from Fe sulfide precursors according to Eq. (3) (Rickard, 1975). Consistent with quantitative phase analysis, pyrite formation was most noticeable over 3–7 days in all experiments (Table S1, Fig. 6c). Ni concentration in solution was systematically lower than its detection limit with AAS (0.05 mg/L – data not shown).

$$FeS + S^0 \rightarrow FeS_2 \quad (3)$$

3.6. Solid chemistry during sulfidation

Content and distribution of Fe, Ni, O, and S within sulfidized particles were determined using HAADF imaging coupled with EDX analysis (Figs. 7 and S5). Fibrous morphologies were ascribed to goethite crystals, whereas bright areas in HAADF dark field micrograph were mainly related to aggregated crystals shown in Figs. 5 and S5 and identified as iron sulfides, consistent with elemental distributions. Both Fe and O were evenly distributed in both types of crystals however, consistent with the formation of Fe sulfides on residual goethite particles. On the other hand, Ni and S appeared to be concentrated in the bright areas, the distributions of the two elements being highly correlated, indicative of the slight Ni enrichment of newly formed iron sulfides compared to residual goethite. For example, Ni mass fraction in selected Fe sulfide polycrystals and goethite crystals (areas #1 and #2, respectively, in Fig. 7 upper left) were 0.9 ± 0.3%, and 0.5 ± 0.2%, respectively.

3.7. Acid Treatment of pristine and sulfidized samples

3.7.1. HCl treatment and kinetic modeling

Fe was steadily released from pristine GtNi6 and GtANi20 upon 3 M HCl treatment and Fe concentration in solution reached a plateau after ~24 hrs (Fig. 8a), even though the former dissolved slightly slower than the latter (inset in Fig. 8a). By contrast, Fe release from their sulfidized counterparts appeared more complex. The initial (~10 mins) Fe release from sulfidized samples is larger than that of their pristine equivalents (inset in Fig. 8a), likely as the result of Fe(II) desorption from mineral surfaces and from the dissolution of FeS_x clusters and MIS. Following this initial fast stage, Fe release from sulfidized samples slowed down from 10 mins to ~12–24 hrs, a period during which goethite dissolution is the main process releasing Fe to solution. In contrast to pristine goethite samples that were thoroughly dissolved after 24 hrs of hydrochloric acid treatment, Fe release from sulfidized samples continued, most likely owing to dissolution of nanocrystalline pyrite at this stage, consistent with the enhanced solubility of fine-grained pyrite in HCl (Cornwell and Morse, 1987). Dissolution of fine-grained pyrite is supported by the overall Fe release during HCl treatment that exceeds the relative proportion of goethite and crystalline MIS determined by XRD in sulfidized samples (~60–67 wt% – Table S1, Fig. S6). These proportions do not account for FeS_x clusters. Fe release rate was significantly decreased however, and no plateau was reached during the HCl treatment of sulfidized samples, even after 96 hrs.

The release of Ni associated to pristine goethite and to corresponding sulfidized samples differed significantly from that of Fe in these phases but also from one sample to the other (Fig. 8b). For example, Ni in GtNi6 was released slightly faster than Fe, both metals reaching a maximum concentration after ~24 hrs and complete goethite dissolution. In contrast, most adsorbed Ni present in GtANi20 was quickly released to the solution (~76% after 5 mins of the HCl acidic treatment) before reaching a plateau after ~7 hrs. Their sulfidized counterparts (GtNi6-44d and GtANi20-44d) exhibited contrasting Ni release rates before and after ~10 mins of interaction with HCl (inset in Fig. 8b), consistent with Fe release. In particular, ~25% and ~9% of Ni was released from GtNi6-44d and GtANi20-44d, respectively, within the first 10 mins of interaction. After this initial fast release, which likely represents Ni associated to FeS_x clusters and MIS, Ni release from both samples appeared steady with no obvious rate modification.

Simulations of Fe and Ni release kinetics during HCl treatment were performed using one-phase exponential decay function to evaluate the relative release of the two metals from pristine and sulfidized samples (Fig. S7, S8, and Table S3). The rates (1st derivative of kinetics) of Fe and Ni released from all the examined samples decreased as a function of time, and the relative release rate of Ni to Fe varied gradually (Fig. S7). For GtANi20, the adsorbed Ni experienced fast release while structural Fe was released gradually, producing an inverted-L relative release curve of Ni to Fe (Fig. 8c). For GtNi6, Ni (~69%) was released faster compared to Fe (~44%) before ~4.30 hrs and slower after that, yielding a convex relative release curve (Figs. 8c and S7), indicating a non-

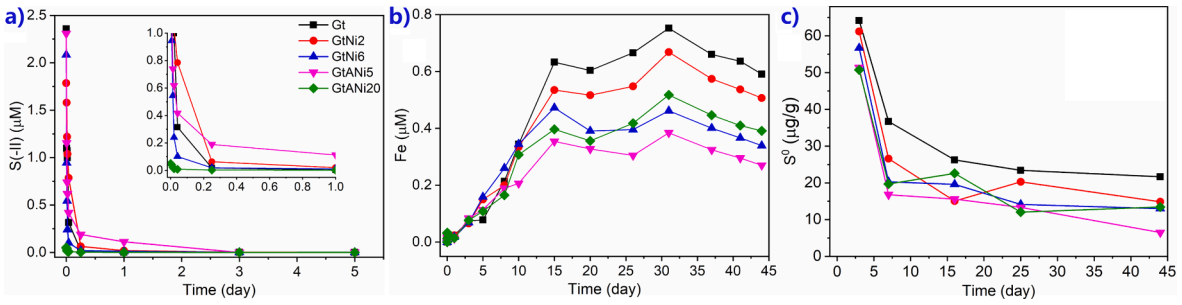

Fig. 6. Evolution of (a) S(-II) and (b) Fe(II) concentration in solution and (c) relative mass of elemental sulfur (S^0) associated with the solids as a function of sulfidation time for Ni-free/-bearing goethites. S^0 content was quantified only for sulfidized samples.

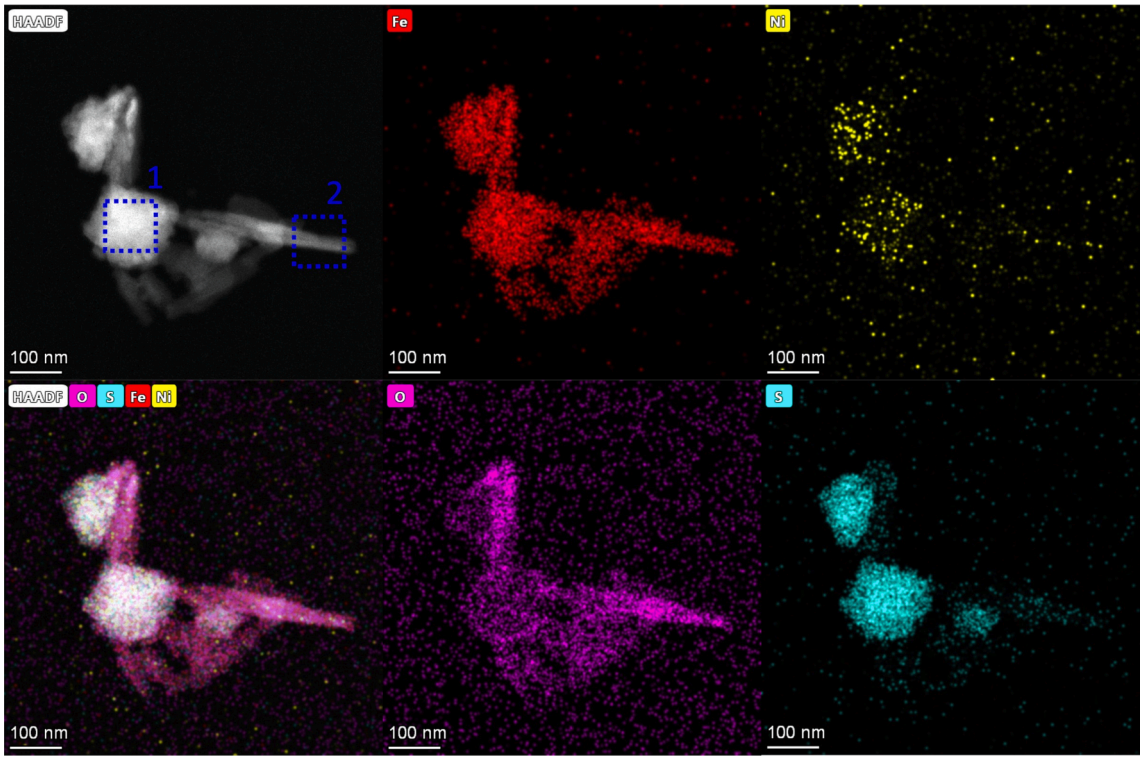

Fig. 7. STEM/HAADF micrograph (upper left) and EDX maps for Fe (upper center), Ni (upper right), O (lower center), S (lower right), and composite Fe-Ni-S-O image obtained for GtANi20-44d.

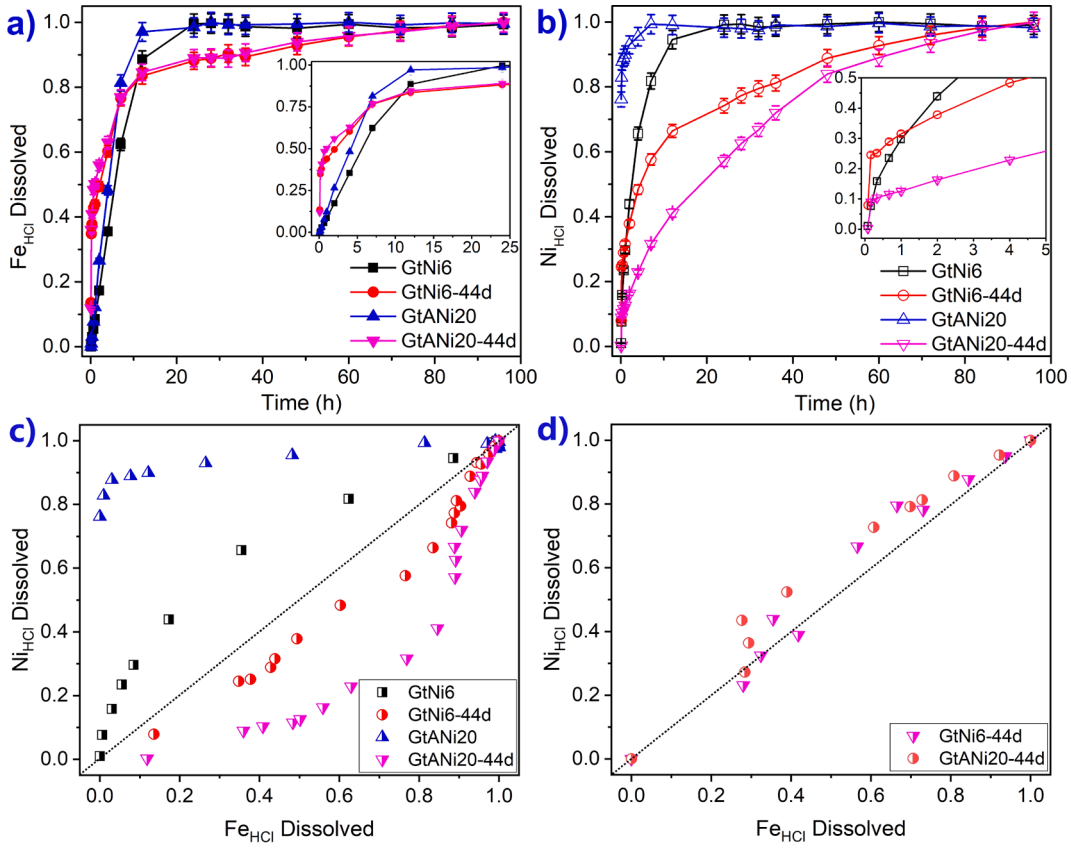

Fig. 8. Kinetic release of (a) Fe and (b) Ni during HCl treatment of pristine GtNi6 and GtANi20 and of their sulfidized counterparts. (c) Congruency of Ni versus Fe release during HCl treatment of pristine GtNi6 and GtANi20 and of their sulfidized counterparts during the whole treatment. (d) Congruency of Ni versus Fe release during HCl treatment of sulfidized samples (GtNi6-44d and GtANi20-44d) excluding data points before 24hrs. The y = x line is plotted as a dotted line in (c) and (d).

uniform distribution of Ni in goethite (Girgin et al., 2011; Landers and Gilkes, 2007; Landers et al., 2009), with a significant Ni-enrichment in goethite outer layers. For sulfidized samples, Fe was released slightly or significantly faster relative to Ni upon the HCl treatment, and the rates dropped until equal to each other at ~9.60 hrs and ~7.10 hrs for GtNi6-44d and GtANi20-44d, respectively (Figs. 8c and S7). Although both sulfidized samples displayed rather similar trends of Fe release (~76% vs. ~78% after 7.70 hrs), Ni was released faster from GtNi6-44d than from GtANi20-44d before ~7.70 hrs (~60% vs. ~33%, Fig. S8). Interestingly, both sulfidized samples led to a concave relative release curve (Fig. 8c), that of GtNi6-44d being close to the y = x line. In contrast, that of GtANi20-44d was far from the line, indicating that Ni was more homogeneously distributed in GtNi6-44d compared to that in GtANi20-44d. In addition, GtANi20-44d most likely contained more Ni-free/poor phase(s) (residual goethite mainly) that were readily extracted by HCl and Ni-rich cores. The two sulfidized samples contained multiple Fe species [i.e., adsorbed Fe(II), goethite, FeS_x clusters, greigite, mackinawite, and pyrite], each likely releasing Fe at a different rate, especially during the first ~24 hrs of the treatment. To overcome this issue, the relative release curve was plotted excluding data points measured during this initial 24 hrs period (Fig. 8d). This curve was close to the y = x line, indicating Ni was homogeneously distributed in nanocrystalline pyrite.

3.7.2. HNO_3 treatment

When sulfidized samples pre-treated with HCl were equilibrated in 2 M HNO_3, the release of Fe and Ni proceeded (Fig. 9), accounting for the sole pyrite dissolution. For both GtNi6-44d and GtANi20-44d, Fe release rate was significantly enhanced by HNO_3 treatment, and reached plateaus after ~48–72 hrs. Ni release was strongly correlated to that of Fe, leading to an almost linear relative release curve (Fig. 9c), indicative of a homogeneous Ni distribution in pyrite crystals.

4. Discussion

4.1. Mineralogical evolution along goethite sulfidation

In the present study, diffraction (Figs. 1 and S1), electron microscopy (Figs. 5 and S5), and spectroscopic (Figs. 3, S2, and S3) data consistently show that crystalline products of goethite sulfidation consist mainly of pyrite with minor mackinawite and greigite. Sulfidation of goethite and other iron (oxyhydr)oxides thus appears as a pathway possibly accounting for the coexistence of iron (oxyhydr)oxides and of these iron sulfides in natural anoxic or alternating oxic-anoxic sediments and soils (Kalatha and Economou-Eliopoulos, 2015; Otero et al., 2009; Seyfferth et al., 2020). In nature, goethite and iron monosulfide (FeS) prevail in surface or subsurface horizons of soil profiles, whereas pyrite is the major iron-bearing mineral in deep horizons (Kraal et al., 2013; Seyfferth et al., 2020). Experimental studies, including the present one, provide additional insights into specific conditions favoring the formation of one phase or the other, common iron sulfides obtained from goethite sulfidation being amorphous FeS_x clusters, mackinawite, greigite, and pyrite (Table 2). More especially, solution pH, relative abundance of goethite [(Fe(III)] and dissolved sulfides [S(-II)], and reaction duration appear to be responsible for reaction product diversity.

Mackinawite was identified in most studies listed in Table 2, and was consistently described as resulting from aging or crystallization of amorphous FeS_x precursors, that would result from direct coprecipitation of Fe(II) and S(-II) according to Eq. (2) (Rickard, 1975; Schoonen and Barnes, 1991a). Both lower (<7.0) pH conditions (Wang and Morse, 1996) and decreased Fe:S(-II) ratios (Kumar et al., 2018) increase dissolution rate of iron (oxyhydr)oxides and mackinawite precipitation rate. Although mackinawite readily precipitates in all runs of the present study, it hardly accumulates during sulfidation, compared to greigite and pyrite (Fig. 2 and Table S1). Two hypotheses may account for this specific behavior: i) the swift consumption of dissolved S(-II) (Fig. 6a) leads to low S(-II) levels, insufficient to precipitate mackinawite but allowing pyrite formation to proceed (Rickard and Luther, 2007); ii) mackinawite acts as a precursor for the formation of both greigite and pyrite (Wang and Morse, 1996). In addition, the initial formation of mackinawite provides active surfaces that favor pyrite nucleation and growth (Rickard and Luther, 2007), inhibiting further mackinawite formation and growth. Mackinawite was also reported to be a necessary precursor for greigite formation (Rickard and Luther, 2007) through a rearrangement of Fe atoms in a [S(-II)] cubic close packing lattice and Fe loss to reach a proper Fe:S ratio (Lennie et al., 1997).

Formation of greigite along goethite sulfidation derived from XRD data analysis in the present work (Fig. 1) was consistently reported only by Wang and Morse (1996) in similar sulfidation experiments. In contrast, the presence of greigite was rejected in other studies from the analysis of Mössbauer spectra (Wan et al., 2017) or from the modeling of S K-edge XANES (X-ray absorption near edge structure) data (Kumar et al., 2018). These contrasting results suggest the key role of initial solution pH for greigite formation; sulfidation experiments of Wang and Morse (1996) were performed indeed under weakly acidic conditions consistent with the present ones (pH = 5.0 and 6.0, respectively), whereas those of Wan et al. (2017) and Kumar et al. (2018) were performed under circum-neutral conditions (pH = 7.0 or 7.2). Contrary to the present hypothesis derived from the comparison of experimental studies, Son et al. (2022) predicted from Density Functional Theory calculations that greigite stability and formation would be favored by higher pH conditions. These calculations were performed however for nanometer sized particles (~0.5–4 nm) to benefit from greigite lower surface energy compared to pyrite. In the present study, Rietveld refinement of XRD data indicates much larger crystal sizes (~15–18 nm along the 001 axis) for greigite. The Fe:S ratio appears less influential for greigite precipitation as Kumar et al. (2018) performed their experiments using a Fe:S ratio similar to that of the present study (Fe:S molar ratio ≈ 1).

Pyrite was formed in most goethite sulfidation experiments reported

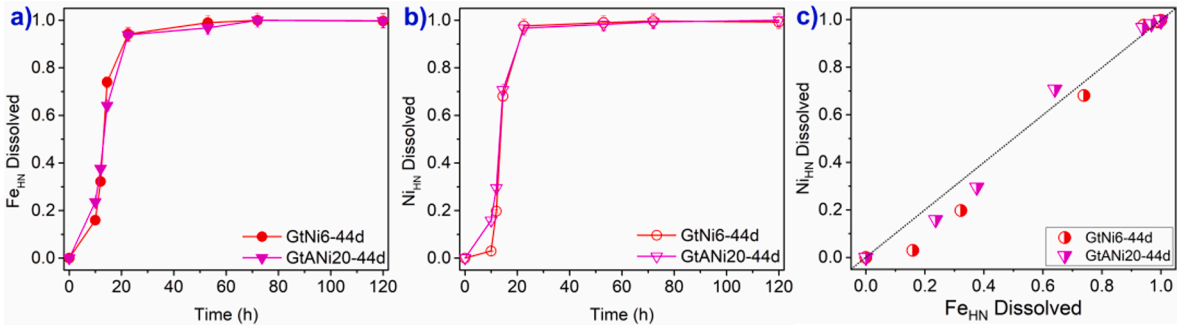

Fig. 9. Kinetic release of (a) Fe and (b) Ni during HNO_3 treatment of HCl-treated sulfidized GtNi6-44d and GtANi20-44d. (c) Congruency of Ni versus Fe release during HNO_3 treatment of HCl-treated sulfidized GtNi6-44d and GtANi20-44d. The y = x line is plotted as a dotted line in (c).

Table 2
Conditions of goethite reaction with S(-II) and mineralogy of iron sulfides reported in the literature and in the present study.

c_{Fe}	$c_{S(-II)}$	Fe:S	pH	Reaction Duration	Products	Identification Methods	References
11.20	50.00	0.22	7.77	~2 hrs	amorphous FeS_x, mackinawite	XRD	Rickard, 1974
11.20	100.00	0.11	7.64				
11.20	200.00	0.06	7.50				
11.20	400.00	0.03	7.24				
11.20	500.00	0.02	6.95				
1.12	4.50	0.25	7.55	~24 hrs	iron monosulfide	chemical method	Pyzik and Sommer, 1981
5.10	4.16	1.23	7.61				
1.04	4.90	0.21	7.54				
3.17	2.60	1.22	7.54				
1.06	5.50	0.19	7.42				
1.06	5.40	0.20	7.40				
n.i.	17.40	**	5.12	~2160 hrs	mackinawite, greigite, pyrite	XRD, SEM	Wang and Morse, 1996
n.i.	17.60		5.06	~4320 hrs			
n.i.	66.50		5.01	~4320 hrs			
41.60	8.10	5.14	7.00	~168 hrs	mackinawite, pyrite	Mössbauer spectroscopy	Wan et al., 2017
3.40	14.90	0.23	7.00	~3672 hrs			
112.36	224.72	0.50	7.20	~336 hrs	mackinawite	XANES	Kumar et al., 2018
112.36	112.36	1.00			mackinawite		
11.20	11.20	1.00	6.00	~1056 hrs	mackinawite, greigite, pyrite	XRD, SEM, TEM	This study

Note: c_{Fe} and $c_{S(-II)}$ are given in mM. "n.i." stands for "not indicated", and ** indicates "S(-II) in excess".

in the literature. Slightly alkaline conditions and low Fe:S(-II) ratios appear however to hamper pyrite formation (Kumar et al., 2018; Pyzik and Sommer, 1981; Rickard, 1974; Wan et al., 2017). Duration of the sulfidation experiment also appears as an important parameter for pyrite formation. Pyrite was not detected by Rickard (1974) and Pyzik and Sommer (1981) whose goethite sulfidation experiments lasted ~2 and ~24 hrs, respectively, whereas a minor amount of pyrite (~1–2%) was detected only after ~48 hrs by Wan et al. (2017) using Mössbauer spectroscopy, consistent with the present study in which minor pyrite (~1–2 wt%) was detected in sulfidation products after 3 days (Figs. 2, 3, and S1). In the present sulfidation experiments, pyrite formed massively from 3 to 7 days (Figs. 2, 3, S1, and S2). Low Fe:S(-II) ratios (≤0.2) may delay further pyrite formation as shown by the presence of pyrite being detected only after ~56–60 days under such experimental conditions (Wan et al., 2017; Wang and Morse, 1996). Despite favorable Fe:S(-II) ratio (0.5–1.0) and sufficient duration (14 days), Kumar et al. (2018) discarded pyrite presence among goethite sulfidation products from the analysis of S K-edge XANES data. Contrasting initial solution pH values (7.2 vs. 6.0 in the present experiments) are most likely responsible for the much higher pyrite contents reported in the present experiments (~28.5–39.1% after 7–25 days – Fig. 2 and Table S1), consistent with the results of Wang and Morse (1996). Although pyrite is the dominant iron sulfide in most geological settings, Fe sulfidation or pyritization appears incomplete in many cases, with the persistence of MIS. Apart from the unfavorable conditions described above [low Fe:S(-II) ratio, slightly alkaline pH conditions], low concentration of S^0 in solution (Fig. 6c) may also hamper MIS transformation to pyrite Wang and Morse (1996).

Consistently, colloidal FeS (or FeS_x clusters) were readily formed upon addition of goethite into the S(-II)-containing solutions, as the solution got black immediately after the addition (Hellige et al., 2012; Hockmann et al., 2020; Noël et al., 2020; Peiffer et al., 2015; Rickard, 1974), even after filtration through 0.22 μm nylon filters (not shown). Solutions remained black-colored for about one week before turning colorless consistent with previous observations from ferrihydrite sulfidation (Noël et al., 2020). The timing of this color change roughly coincides with the remarkable decrease of S^0 (Fig. 6c) and with the onset of the three crystalline iron sulfides identified by XRD in the present experiments (Fig. 2 and Table S1). This coincidence suggests that reaction between colloidal FeS (or FeS_x clusters) and S^0 according to Eq. (2) most likely contributed to or even dominated the early formation of pyrite from goethite sulfidation (Hellige et al., 2012; Peiffer et al., 2015).

4.2. *Influence of Ni on the sulfidation of goethite to pyrite*

In this study, the influence of both adsorbed and structurally incorporated Ni on/in goethite on its sulfidation was assessed. The limited modification of Fe local environment in sulfidized Ni-bearing samples compared to Ni-free one (Fig. 3, S2, and S3) and the slower formation of pyrite (Fig. S1, Table S1) suggest that the presence of Ni hampered goethite sulfidation. Consistently, after 44 days of interaction with S(-II), reaction products of Ni-free goethite contain significantly more pyrite (54.4% vs. 33.2%, 33.5%, 33.0%, and 40.7%, Table S1) and less MIS (4.2% vs. 12.7%, 12.7%, 16.5%, and 11.7%, Table S1) than their counterparts from Ni-bearing goethites. A similar trend may be observed after 25 days of reaction (Fig. 2 and Table S1), suggesting that Ni stabilized MIS and delayed their complete conversion to pyrite, consistent with previous report (Swanner et al., 2019).

After the swift pyrite formation from 3 to 7 days in both Ni-free and -containing experiments, pyrite formation proceeded gradually (Fig. 2 and Table S1), indicating that MIS likely mediated this process at this later stage (Luther, 1991; Rickard and Luther, 2007), as colloidal FeS and FeS_x clusters almost disappeared. During the pyritization process, destabilization of both FeS_x clusters/colloidal FeS and MIS release Fe(II), likely contributing to the increase of [Fe(II)] in solution within the first ~15 days of reaction [Fig. 6b - (Butler and Rickard, 2000; Lennie et al., 1997)]. For all runs, the content of MIS was kept at a relatively low level (<2.7%) before 7 days, while after that MIS in Ni-containing groups accumulated up to 11.7%–16.6%. In contrast, MIS content in the Ni-free experiment only reached 4.2%, suggesting again that their association with Ni hindered the conversion of MIS to pyrite after 7 days.

The negative impact of Ni on MIS transformation to pyrite started earlier however. After 3 days of interaction with S(-II), iron sulfide formation is extremely marginal in all cases but modification of Fe local environment appears to be more limited in Ni-bearing goethites compared to Gt (Fig. S3). This reduced modification suggests also that the presence of Ni, both as adsorbed and incorporated species, decreases goethite reactivity towards S(-II). As proposed previously (Xu et al., 2006), the presence of Ni(II) sorbed at the goethite surface possibly hinders subsequent sorption of other ions [S(-II) in this study]. In

addition, the reduced surface charge resulting from Ni(II)-for-Fe(III) substitutions could also contribute to decrease goethite reactivity (de Carvalho-E-Silva et al., 2002). It should be noted however that in the present study similar kinetics of S(-II) consumption was measured for all reacting samples up to 3 days (Fig. 6a). This apparent inconsistency likely results from the fast decrease of S(-II) content originating from S (-II) adsorption to goethite surface, precipitation with Fe(II) and Ni (II), and formation of colloidal FeS and FeS_x clusters, making adsorption specific contribution difficult to differentiate.

Mackinawite and FeS_x cluster formation is considered to result from the direct coprecipitation of Fe(II) with S(-II) (Rickard and Luther, 2007), and dissolved Ni(II) precipitates more readily with S(-II) compared to Fe(II) [5.89×10^{-10} vs. 2.29×10^{-4} for Ni and Fe, respectively – (Morse and Arakaki, 1993)]. The tendency of Ni to precipitate first as Ni-rich nuclei has been confirmed recently from TEM observations (Mansor et al., 2019), consistent with the present distribution of Ni in MIS particles (Figs. 7 and S5). In addition, mackinawite crystal growth rate increases in the presence of Ni(II), crystal structure being stabilized by Ni(II) (Ikogou et al., 2017). In the present work, mackinawite content remains limited in all experiments although the maximum mackinawite content [8.0(2) wt.%] was reported for GtANi20-44d (Table S1). The presence of Ni(II) appears to stabilize MIS as a whole (Fig. 2 and Table S1) however, possibly inhibiting their conversion to pyrite. The limited mackinawite content also suggests that the mackinawite-to-greigite transformation was not significantly hindered by Ni thus hampering the identification of a possible positive effect on mackinawite formation.

4.3. The migration of Ni from goethite to iron sulfides

The systematic correlation between Ni and Fe sulfide polycrystals observed with electron microscopy (Figs. 7 and S5) evidenced the migration of Ni initially associated to goethite to iron sulfides (pyrite mainly) resulting from the sulfidation thereof. Acid treatments using HCl suggest however that Ni distribution within MIS depends on the initial association mode of Ni with goethite. When initially incorporated in goethite structure, Ni is homogeneously distributed in newly formed sulfides whereas Ni appears to be enriched in MIS crystal cores when initially adsorbed onto goethite (Fig. 8c), consistent with previous reports (Mansor et al., 2019). In contrast, subsequent acid treatments using HNO_3 indicate that Ni was homogeneously distributed in newly formed pyrite, regardless of the initial association mode of Ni with goethite (Fig. 9c). It should be noted that Ni was not detected in solution during sulfidation of Ni-bearing goethite, implying that this process does not contribute Ni to sedimentary pore water in geological settings. In addition, the absence of dissolved Ni suggests that contrasting Ni distributions observed as a function of the initial association mode of Ni with goethite derive from differences in Ni and Fe release rates during the sulfidation of goethites. Specifically, adsorbed Ni(II) is most likely released faster compared to structural Fe, the latter being gradually released during goethite reductive dissolution. In addition, Ni(II) precipitates with S(-II) faster than Fe(II) (Morse and Arakaki, 1993) and thus concentrates mainly in the inner part of mackinawite particles. In contrast, Ni(II) structurally incorporated in GtNi6 was released almost stoichiometrically with Fe(II), resulting in a homogeneous distribution of both metals within MIS crystals.

Although Ni(II) may be heterogeneously distributed within MIS crystals, its distribution within pyrite systematically appears to be homogeneous as suggested by the congruent release of Ni and Fe along the late (>24 hrs) HCl and the whole HNO_3 acid treatments (Fig. 9c). This homogenous distribution in pyrite appears logical when MIS precursors also exhibit a homogeneous Ni distribution, owing to Fe(II) and Ni(II) interaction with S_2(-II) onto mackinawite and greigite active surfaces to form pyrite (Rickard and Luther, 2007). In MIS formed from Ni-adsorbed goethite, Ni distribution is heterogeneous however, and redistribution of Ni between mackinawite and greigite most likely accounts for this apparent inconsistency. Specifically, mackinawite-to-greigite conversion is likely responsible for this redistribution before the subsequent formation of pyrite, as this conversion was described as the rearrangement of Fe (and Ni in the present study) atoms in a cubic close packing S (-II) lattice (Rickard and Luther, 2007). As a consequence and although a direct mackinawite-to-pyrite conversion was proposed (Rickard, 1975), the formation of a greigite intermediate appears to be an efficient alternative pathway for pyrite formation from mackinawite, greigite occurrence increasing significantly pyrite formation rate (Lennie et al., 1997; Wang and Morse, 1996).

4.4. Geochemical and environmental implications

In natural soil environments, Ni concentration usually increases with increasing depth (Michopoulos, 2021), goethite [and other iron (oxyhydr)oxides] and iron sulfides being common Fe-bearing minerals in upper and deeper horizons, respectively, both being Ni sinks (Ikogou et al., 2017; Morin et al., 2017; Swanner et al., 2019). Goethite is the main Ni host in oxide-type laterite deposits, which accounts for ~70% of Ni world's resources (Landers et al., 2009), the remaining ~30% being hosted in sulfide deposits. Although structural Ni incorporation usually prevails over surface complexation in both cases, Ni release to solution and/or transport to other phases can occur as the result of mineral dissolution or alteration under oxidative (Larsen and Postma, 1997; Nesbitt and Muir, 1994) or reductive (Landers and Gilkes, 2007; Landers et al., 2009) conditions. From the present results, Ni association to goethite slows down its possible conversion to Fe sulfides under reducing conditions, possibly accounting for goethite persistence in thermodynamically unfavorable S(-II)-rich conditions. Ni migration from Fe (oxyhydr)oxides to Fe sulfides along goethite sulfidation as reported in the present work most likely represents the main transport pathway for Ni from the oxic zone to the anoxic zone however. In turn, the swift release of Ni to solution upon the oxidative alteration of Ni-bearing Fe sulfides, in acid mine drainage for example, is a key process of Ni geochemical cycling.

5. Conclusions

The mineralogical evolution observed in the present study along goethite sulfidation is consistent with the commonly accepted reaction mechanisms for this process. The mineralogical sequence, and thus mechanisms at play, is similar for both Ni-free and Ni-containing goethites and involves the swift initial formation of colloidal FeS, FeS_x clusters, and metastable iron sulfides (mackinawite and greigite) prior to pyrite formation that is detected after ~3 days of interaction with S(-II). The early (~3–7 days) formation of pyrite originates from the reaction between colloidal FeS, FeS_x clusters, and S^0, and the later stage (~7–44 days) mainly comes from the conversion of metastable iron sulfides. Consistent with previous reports, greigite formation appears to be favored by slightly acidic pH conditions (pH = 6.0). These conditions also enhance pyrite crystallization, whereas low Fe:S(-II) ratios ($\leq$0.2) negatively impact pyrite formation. Compared to the Ni-free system, pyrite formation rate is also decreased by the presence of Ni, independent of its association mode with goethite, i.e., adsorption or isomorphic substitution. Ni appears indeed to reduce the reactivity of goethite to S (-II) and increase MIS stability, the overall sulfidation progress, as measured by Fe local environment and the relative proportion of sulfides and goethite, being similar in all cases. Incorporation of Ni in intermediate MIS also buffers its subsequent release and induces a uniform distribution of this element in newly formed pyrite, independent of its initial association mode with goethite.

Research Data

Research Data related to this article includes: Chemical compositions; XRD data; XAS data at Fe K-edges; TGA data; Solution chemistry;

Fe/Ni release upon HCl/HNO_3 treatment. Dataset can be accessed at Mendeley Data, V1, https://doi.org/10.17632/khhhyhhkjz.1.

Declaration of Competing Interest

The authors declare that they have no known competing financial interests or personal relationships that could have appeared to influence the work reported in this paper.

Acknowledgements

This work is supported by the National Natural Science Foundations of China (No. 42107319, 42225704, and 42077290). We are grateful to Dr. Zhongjun Chen and Dr. Yunpeng Liu at BSRF for their assistance with Fe K-edge XAFS data collection and analysis, and we thank Dr. Jiang Xu at Zhejiang University for providing XAFS standards of pyrite and mackinawite, and Dr. Shuang Zhang at Huazhong Agricultural University is appreciated for her help with XRD data collection. Dr. Vincent Noël kindly provided the EXAFS reference spectrum of colloidal FeS. ISTerre is part of Labex OSUG@2020 (ANR10-LABX56).

Appendix A. Supplementary material

Supplementary material includes i) XRD patterns showing the mineralogical evolution of goethite samples as a function of sulfidation duration and results of Rietveld refinements performed on this data (quantitative phase analysis and unit-cell parameters of the main minerals present), ii) Fe K-edge EXAFS spectra of pritsine and sulfidized goethite samples and difference thereof, iii) TEM micrographs, SAED, and STEM-HAADF data obtained on sulfidized samples, and iv) modeling of Fe and Ni kinetic release upon HCl treatment of goethite samples. Supplementary material to this article can be found online at https://doi.org/10.1016/j.gca.2023.06.001.

References

Bagarinao, T., 1992. Sulfide as an environmental factor and toxicant: tolerance and adaptations in aquatic organisms. Aquat. Toxicol. 24, 21–62.
Biber, M.V., dos Santos, A.M., Stumm, W., 1994. The coordination chemistry of weathering: IV. Inhibition of the dissolution of oxide minerals. Geochim. Cosmochim. Acta 58, 1999–2010.
Bishop, D.W., Thomas, P.S., Ray, A.S., 1999. α-β Phase Re-Transformation Kinetics in Nickel Sulphide. J. Therm. Anal. Calorim. 56, 429–435.
Burton, E.D., Johnston, S.G., Watling, K., Bush, R.T., Keene, A.F., Sullivan, L.A., 2010. Arsenic effects and behavior in association with the Fe(II)-catalyzed transformation of schwertmannite. Environ. Sci. Technol. 44, 2016–2021.
Butler, I.B., Rickard, D., 2000. Framboidal pyrite formation via the oxidation of iron (II) monosulfide by hydrogen sulphide. Geochim. Cosmochim. Acta 64, 2665–2672.
Canfield, D.E., 1989. Reactive iron in marine sediments. Geochim. Cosmochim. Acta 53, 619–632.
Canfield, D.E., Raiswell, R., Bottrell, S.H., 1992. The reactivity of sedimentary iron minerals toward sulfide. Am. J. Sci. 292, 659–683.
Cao, F., Hu, W., Zhou, L., Shi, W., Song, S., Lei, Y., Wang, S., Zhang, H., 2009. 3D Fe3S4 flower-like microspheres: high-yield synthesis via a biomolecule-assisted solution approach, their electrical, magnetic and electrochemical hydrogen storage properties. Dalton Trans.
Cline, J.D., 1969. Spectrophotometric determination of hydrogen sulfide in natural waters1. Limnol. Oceanogr. 14, 454–458.
Cooper, D.C., Morse, J.W., 1998. Extractability of metal sulfide minerals in acidic solutions: application to environmental studies of trace metal contamination within anoxic sediments. Environ. Sci. Technol. 32, 1076–1078.
Cornell, R.M., 1991. Simultaneous incorporation of Mn, Ni and Co in the goethite (alpha-FeOOH) structure. Clay Miner. 26, 427–430.
Cornell, R.M., Schwertmann, U., 2004. The Iron Oxides: Structure, Properties, Reactions, Occurences and Uses, Second Edition.
Cornwell, J.C., Morse, J.W., 1987. The characterization of iron sulfide minerals in anoxic marine sediments. Mar. Chem. 22, 193–206.
de Carvalho-E-Silva, M.L.M., Partiti, C.S.M., Enzweiler, J., Petit, S., Netto, S.M., de Oliveira, S.M.B., 2002. Characterization of Ni-containing goethites by Mossbauer spectroscopy and other techniques. Hyperfine Interact. 142, 559–576.
Deoliveira, S.M.B., Trescases, J.J., Melfi, A.J., 1992. Lateritic Nickel deposits of Brazil. Miner. Deposita 27, 137–146.
Döbelin, N., 2015. Interlaboratory study on the quantification of calcium phosphate phases by Rietveld refinement. Powder Diffr. 30, 231–241.
Döbelin, N., Kleeberg, R., 2015. Profex: a graphical user interface for the Rietveld refinement program BGMN. J. Appl. Crystallogr. 48, 1573–1580.
Dos Santos, A.M., Stumm, W., 1992. Reductive dissolution of iron(III) (hydr)oxides by hydrogen sulfide. Langmuir 8, 1671–1675.
Du, R., Xian, H., Wu, X., Zhu, J., Wei, J., Xing, J., Tan, W., He, H., 2021. Morphology dominated rapid oxidation of framboidal pyrite. Geochem. Perspect. Let. 16, 53–58.
Dubbin, W.E., Bullough, F., 2017. Dissolution of Al-Substituted Goethite in the Presence of Ferrichrome and Enterobactin at pH 6.5. Aquat. Geochem. 23, 61–74.
Dublet, G., Juillot, F., Morin, G., Fritsch, E., Fandeur, D., Ona-Nguema, G., Brown Jr., G. E., 2012. Ni speciation in a New Caledonian lateritic regolith: a quantitative X-ray absorption spectroscopy investigation. Geochim. Cosmochim. Acta 95, 119–133.
Dublet, G., Juillot, F., Morin, G., Fritsch, E., Fandeur, D., Brown Jr., G.E., 2015. Goethite aging explains Ni depletion in upper units of ultramafic lateritic ores from New Caledonia. Geochim. Cosmochim. Acta 160, 1–15. %@ 0016–7037.
Dunn, J.G., Kelly, C.E., 1977. A TG/DTA/MS study of the oxidation of nickel sulphide. J. Therm. Anal. 12, 43–52.
Elias, M., 2002. Nickel laterite deposits – geological overview, resources and exploitation.
Eliopoulos, D.G., Economou-Eliopoulos, M., 2000. Geochemical and mineralogical characteristics of Fe–Ni- and bauxitic-laterite deposits of Greece. Ore Geol. Rev. 16, 41–58.
Fadrus, H., Malý, J., 1975. Suppression of iron(III) interference in the determination of iron(II) in water by the 1,10-phenanthroline method. Analyst 100, 549–554.
Fan, R., Gerson, A.R., 2015. Synchrotron micro-spectroscopic examination of Indonesian nickel laterites. Am. Mineral. 100, 926–934.
Frierdich, A.J., McBride, A., Tomkinson, S., Southall, S.C., 2019. Nickel cycling and negative feedback on Fe(II)-catalyzed recrystallization of goethite. ACS Earth Space Chem. 3, 1932–1941.
Gasser, U.G., Jeanroy, E., Mustin, C., Barres, O., Nuesch, R., Berthelin, J., Herbillon, A.J., 1996. Properties of synthetic goethites with Co for Fe substitution. Clay Miner. 31, 465–476.
Girgin, I., Obut, A., Ucyildiz, A., 2011. Dissolution behaviour of a Turkish lateritic nickel ore. Miner. Eng. 24, 603–609.
Hellige, K., Pollok, K., Larese-Casanova, P., Behrends, T., Peiffer, S., 2012. Pathways of ferrous iron mineral formation upon sulfidation of lepidocrocite surfaces. Geochim. Cosmochim. Acta 81, 69–81.
Hockmann, K., Planer-Friedrich, B., Johnston, S.G., Peiffer, S., Burton, E.D., 2020. Antimony mobility in sulfidic systems: Coupling with sulfide-induced iron oxide transformations. Geochim. Cosmochim. Acta 282, 276–296.
Hohmann, C., Morin, G., Ona-Nguema, G., Guigner, J.M., Brown, G.E., Kappler, A., 2011. Molecular-level modes of As binding to Fe(III) (oxyhydr)oxides precipitated by the anaerobic nitrate-reducing Fe(II)-oxidizing Acidovorax sp strain BoFeN1. Geochim. Cosmochim. Acta 75, 4699–4712.
Huang, F.-G., Jia, S.-Y., Liu, Y., Wu, S.-H., Han, X., 2015. Reductive dissolution of ferrihydrite with the release of As(V) in the presence of dissolved S(-II). J. Hazard. Mater. 286, 291–297.
Huerta-Diaz, M.A., Morse, J.W., 1990. A quantitative method for determination of trace metal concentrations in sedimentary pyrite. Mar. Chem. 29, 119–144.
Hurtgen, M.T., Lyons, T.W., Ingall, E.D., Cruse, A.M., 1999. Anomalous enrichments of iron monosulfide in euxinic marine sediments and the role of H2S in iron sulfide transformations: Examples from Effingham Inlet, Orca Basin, and the Black Sea. Am. J. Sci. 299, 556–588.
Ikogou, M., Ona-Nguema, G., Juillot, F., Le Pape, P., Menguy, N., Richeux, N., Guigner, J. M., Noel, V., Brest, J., Baptiste, B., Morin, G., 2017. Long-term sequestration of nickel in mackinawite formed by Desulfovibrio capillatus upon Fe(III)-citrate reduction in the presence of thiosulfate. Appl. Geochem. 80, 143–154.
Islam, M., Patel, R., 2017. Solvothermal synthesis of greigite (Fe3S4)- Conducting polypyrrole nanocomposite and its application towards arsenic removal. Sep. Sci. Technol. 52, 2835–2852.
Kalatha, S., Economou-Eliopoulos, M., 2015. Framboidal pyrite and bacterio-morphic goethite at transitional zones between Fe-Ni-laterites and limestones: Evidence from Lokris, Greece. Ore Geol. Rev. 65, 413–425.
Kraal, P., Burton, E.D., Bush, R.T., 2013. Iron monosulfide accumulation and pyrite formation in eutrophic estuarine sediments. Geochim. Cosmochim. Acta 122, 75–88.
Krs, M., Novak, F., Krsova, M., Pruner, P., Jansa, J., 1993. Magnetic-properties, self-reversal remanence and thermal alteration products of smythite. Stud. Geophys. Geod. 37, 382–400.
Kumar, N., Pacheco, J.L., Noel, V., Dublet, G., Brown, G.E., 2018. Sulfidation mechanisms of Fe(III)-(oxyhydr)oxide nanoparticles: a spectroscopic study. Environ. Sci. Nano 5, 1012–1026.
Kyprianidou-Leodidou, T., Althaus, H.J., Wyser, Y., Vetter, D., Buchler, M., Caseri, W., Suter, U.W., 1997. High refractive index materials of iron sulfides and poly(ethylene oxide). J. Mater. Res. 12, 2198–2206.
Lan, Y., Butler, E.C., 2014. Monitoring the transformation of mackinawite to greigite and pyrite on polymer supports. Appl. Geochem. 50, 1–6.
Landers, M., Gilkes, R.J., 2007. Dehydroxylation and dissolution of nickeliferous goethite in New Caledonian lateritic Ni ore. Appl. Clay Sci. 35, 162–172.
Landers, M., Gilkes, R.J., Wells, M., 2009. Dissolution kinetics of dehydroxylated nickeliferous goethite from limonitic lateritic nickel ore. Appl. Clay Sci. 42, 615–624.
Larsen, F., Postma, D., 1997. Nickel mobilization in a groundwater well field: release by pyrite oxidation and desorption from manganese oxides. Environ. Sci. Technol. 31, 2589–2595.
Larsen, O., Postma, D., 2001. Kinetics of reductive bulk dissolution of lepidocrocite, ferrihydrite, and goethite. Geochim. Cosmochim. Acta 65, 1367–1379.

Lennie, A.R., Redfern, S.A.T., Champness, P.E., Stoddart, C.P., Schofield, P.F., Vaughan, D.J., 1997. Transformation of mackinawite to greigite: An in situ X-ray powder diffraction and transmission electron microscope study. Am. Mineral. 82, 302–309.
Liu, J., Pellerin, A., Wang, J., Rickard, D., Antler, G., Zhao, J., Wang, Z., Jørgensen, B.B., Ono, S., 2022. Multiple sulfur isotopes discriminate organoclastic and methane-based sulfate reduction by sub-seafloor pyrite formation. Geochim. Cosmochim. Acta 316, 309–330.
Lowers, H.A., Breit, G.N., Foster, A.L., Whitney, J., Yount, J., Uddin, N., Muneem, A., 2007. Arsenic incorporation into authigenic pyrite, bengal basin sediment, Bangladesh. Geochim. Cosmochim. Acta 71, 2699–2717.
Luther, G.W., 1991. Pyrite synthesis via polysulfide compounds. Geochim. Cosmochim. Acta 55, 2839–2849.
Manceau, A., Schlegel, M.L., Musso, M., Sole, V.A., Gauthier, C., Petit, P.E., Trolard, F., 2000. Crystal chemistry of trace elements in natural and synthetic goethite. Geochim. Cosmochim. Acta 64, 3643–3661.
Mansor, M., Winkler, C., Hochella Jr., M.F., Xu, J., 2019. Nanoparticulate Nickel-Hosting Phases in Sulfidic Environments: Effects of Ferrous Iron and Bacterial Presence on Mineral Formation Mechanism and Solid-Phase Nickel Distribution. Front. Earth Sci. 7.
Maurice, P.A., Lee, Y.J., Hersman, L.E., 2000. Dissolution of Al-substituted goethites by an aerobic Pseudomonas mendocina var. bacteria. Geochim. Cosmochim. Acta 64, 1363–1374.
Michopoulos, P., 2021. Nickel in forests - a short review on its distribution and fluxes. Folia Oecologica 48, 205–214.
Morin, G., Noel, V., Menguy, N., Brest, J., Baptiste, B., Tharaud, M., Ona-Nguema, G., Ikogou, M., Viollier, E., Juillot, F., 2017. Nickel accelerates pyrite nucleation at ambient temperature. Geochem. Perspect. Let. 5, 6–11.
Morse, J.W., Arakaki, T., 1993. Adsorption and coprecipitation of divalent metals with mackinawite (FeS). Geochim. Cosmochim. Acta 57, 3635–3640.
Morse, J.W., Luther, G.W., 1999. Chemical influences on trace metal-sulfide interactions in anoxic sediments. Geochim. Cosmochim. Acta 63, 3373–3378.
Morse, J.W., Millero, F.J., Cornwell, J.C., Rickard, D., 1987. The chemistry of the hydrogen sulfide and iron sulfide systems in natural waters. Earth Sci. Rev. 24, 1–42.
Nachtegaal, M., Spark, D.L., 2002. Kinetics and mechanisms of nickel surface precipitation in multi-sorbent system: a spectroscopic study. In: 17th WCSS, Thailand, pp. 1345–1355.
Nesbitt, H.W., Muir, I.J., 1994. X-ray photoelectron spectroscopic study of a pristine pyrite surface reacted with water-vapor and air. Geochim. Cosmochim. Acta 58, 4667–4679.
Noël, V., Kumar, N., Boye, K., Barragan, L., Lezama-Pacheco, J.S., Chu, R., Tolic, N., Brown, G.E., Bargar, J.R., 2020. FeS colloids - formation and mobilization pathways in natural waters. Environ. Sci. Nano 7, 2102–2116.
Noël, V., Morin, G., Juillot, F., Marchand, C., Brest, J., Bargar, J.R., Munoz, M., Marakovic, G., Ardo, S., Brown Jr., G.E., 2015. Ni cycling in mangrove sediments from New Caledonia. Geochim. Cosmochim. Acta 169, 82–98.
Otero, X.L., Ferreira, T.O., Huerta-Diaz, M.A., Partiti, C.S.M., Souza, V., Vidal-Torrado, P., Macias, F., 2009. Geochemistry of iron and manganese in soils and sediments of a mangrove system, Island of Pai Matos (Cananeia - SP, Brazil). Geoderma 148, 318–335.
Peiffer, S., Behrends, T., Hellige, K., Larese-Casanova, P., Wan, M., Pollok, K., 2015. Pyrite formation and mineral transformation pathways upon sulfidation of ferric hydroxides depend on mineral type and sulfide concentration. Chem. Geol. 400, 44–55.
Ponomar, V.P., 2018. Thermomagnetic properties of the goethite transformation during high-temperature treatment. Miner. Eng. 127, 143–152.
Poulton, S.W., 2003. Sulfide oxidation and iron dissolution kinetics during the reaction of dissolved sulfide with ferrihydrite. Chem. Geol. 202, 79–94.
Poulton, S.W., Krom, M.D., Raiswell, R., 2004. A revised scheme for the reactivity of iron (oxyhydr)oxide minerals towards dissolved sulfide. Geochim. Cosmochim. Acta 68, 3703–3715.
Pyzik, A.J., Sommer, S.E., 1981. Sedimentary iron monosulfides: Kinetics and mechanism of formation. Geochim. Cosmochim. Acta 45, 687–698.
Ravel, B., Newville, M., 2005. ATHENA and ARTEMIS: interactive graphical data analysis using IFEFFIT. Phys. Scr. 2005, 1007.
Ren, H.-T., Ji, Z.-Y., Wu, S.-H., Han, X., Liu, Z.-M., Jia, S.-Y., 2018. Photoreductive dissolution of schwertmannite induced by oxalate and the mobilization of adsorbed As(V). Chemosphere 208, 294–302.
Rickard, D.T., 1974. Kinetics and mechanism of the sulfidation of goethite. Am. J. Sci. 274, 941–952.
Rickard, D., 1975. Kinetics and mechanism of pyrite formation at low temperatures. Am. J. Sci. 275, 636–652.
Rickard, D., Luther, G.W., 2007. Chemistry of Iron Sulfides. Chem. Rev. 107, 514–562.
Sagnotti, L., Winkler, A., 1999. Rock magnetism and palaeomagnetism of greigite-bearing mudstones in the Italian peninsula. Earth Planet. Sci. Lett. 165, 67–80.
Schoonen, M.A.A., Barnes, H.L., 1991a. Reactions forming pyrite and marcasite from solution: II. Via FeS precursors below 100 °C. Geochim. Cosmochim. Acta 55, 1505–1514.
Schoonen, M.A.A., Barnes, H.L., 1991b. Reactions forming pyrite and marcasite from solution: I. Nucleation of FeS2 below 100°C. Geochim. Cosmochim. Acta 55, 1495–1504.
Seyfferth, A.L., Bothfeld, F., Vargas, R., Stuckey, J.W., Wang, J., Kearns, K., Michael, H. A., Guimond, J., Yu, X., Sparks, D.L., 2020. Spatial and temporal heterogeneity of geochemical controls on carbon cycling in a tidal salt marsh. Geochim. Cosmochim. Acta 282, 1–18.
Son, S., Hyun, S.P., Charlet, L., Kwon, K.D., 2022. Thermodynamic stability reversal of iron sulfides at the nanoscale: Insights into the iron sulfide formation in low-temperature aqueous solution. Geochim. Cosmochim. Acta 338, 220–228.
Suter, D., Banwart, S., Stumm, W., 1991. Dissolution of hydrous Iron(III) oxides by reductive mechanisms. Langmuir 7, 809–813.
Swanner, E.D., Webb, S.M., Kappler, A., 2019. Fate of cobalt and nickel in mackinawite during diagenetic pyrite formation. Am. Mineral. 104, 917–928.
Ugwu, I.M., Sherman, D.M., 2019. The solubility of goethite with structurally incorporated nickel and cobalt: Implication for laterites. Chem. Geol. 518, 1–8.
Ugwu, I.M., Sherman, D.M., Bacon, C.G.D., 2019. Sorption of nickel onto goethite (alpha-FeOOH) and desorption kinetics of aged synthetic Ni-goethite: Implication for Ni laterite ore. Chem. Geol. 509, 223–233.
Wan, M., Schroeder, C., Peiffer, S., 2017. Fe(III): S(-II) concentration ratio controls the pathway and the kinetics of pyrite formation during sulfidation of ferric hydroxides. Geochim. Cosmochim. Acta 217, 334–348.
Wang, Q.W., Morse, J.W., 1996. Pyrite formation under conditions approximating those in anoxic sediments.1. Pathway and morphology. Mar. Chem. 52, 99–121.
Wells, M.A., Fitzpatrick, R.W., Gilkes, R.J., 2006. Thermal and mineral properties of Al-, Cr-, Mn-, Ni- and Ti-substituted goethite. Clays Clay Miner. 54, 176–194.
Xu, Y., Axe, L., Yee, N., Dyer, J.A., 2006. Bidentate complexation modeling of heavy metal adsorption and competition on goethite. Environ. Sci. Technol. 40, 2213–2218.
Yang, F., Lai, Y., Song, Y., 2019. Determination of the influence of pyrite on coal spontaneous combustion by thermodynamics analysis. Process Saf. Environ. Prot. 129, 163–167.
Zachara, J.M., Fredrickson, J.K., Smith, S.C., Gassman, P.L., 2001. Solubilization of Fe (III) oxide-bound trace metals by a dissimilatory Fe(III) reducing bacterium. Geochim. Cosmochim. Acta 65, 75–93.

Supplementary Material to:

Sulfidation of Ni-bearing goethites to pyrite: the effects of Ni and implications for its migration between iron phases

Zhongkuan Wu[a], Tingting Zhang[a], Bruno Lanson[b], Hui Yin[c], Dong Cheng[a], Peng Liu[d], Feng He[a,e,*]

[a]*College of Environment, Zhejiang University of Technology, Hangzhou 310014, China*

[b]*Univ. Grenoble Alpes, Univ. Savoie Mont Blanc, CNRS, IRD, Univ. Gustave Eiffel, ISTerre, F-38000 Grenoble, France*

[c]*Key Laboratory of Arable Land Conservation (Middle and Lower Reaches of Yangtse River), Ministry of Agriculture and Rural Affairs, College of Resources and Environment, Huazhong Agricultural University, Wuhan 430070, China*

[d]*School of Environmental Studies & State Key Laboratory of Biogeology and Environmental Geology, China University of Geosciences, Wuhan 430074, China*

[e]*Institute of Environmental Processes and Pollution Control, and School of Environment and Civil Engineering, Jiangnan University, Wuxi, 214122, China*

Corresponding author.
E-mail address: fenghe@zjut.edu.cn (Feng He).

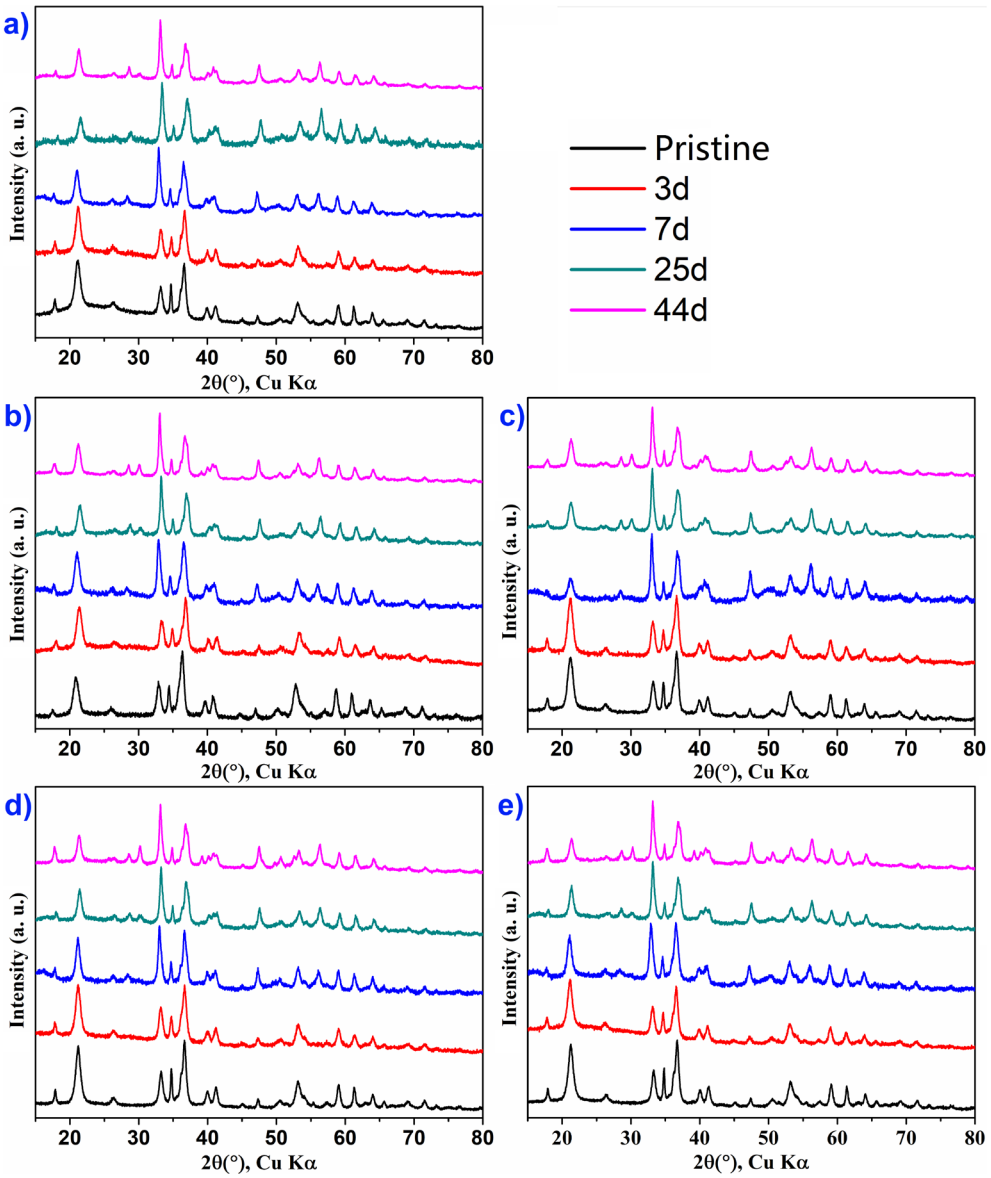

Fig. S1. Evolution of XRD patterns of Ni-free/-containing goethites as a function of sulfidation duration: a): Gt, b): GtNi2, c): GtNi6, d): GtANi5, and e): GtANi20.

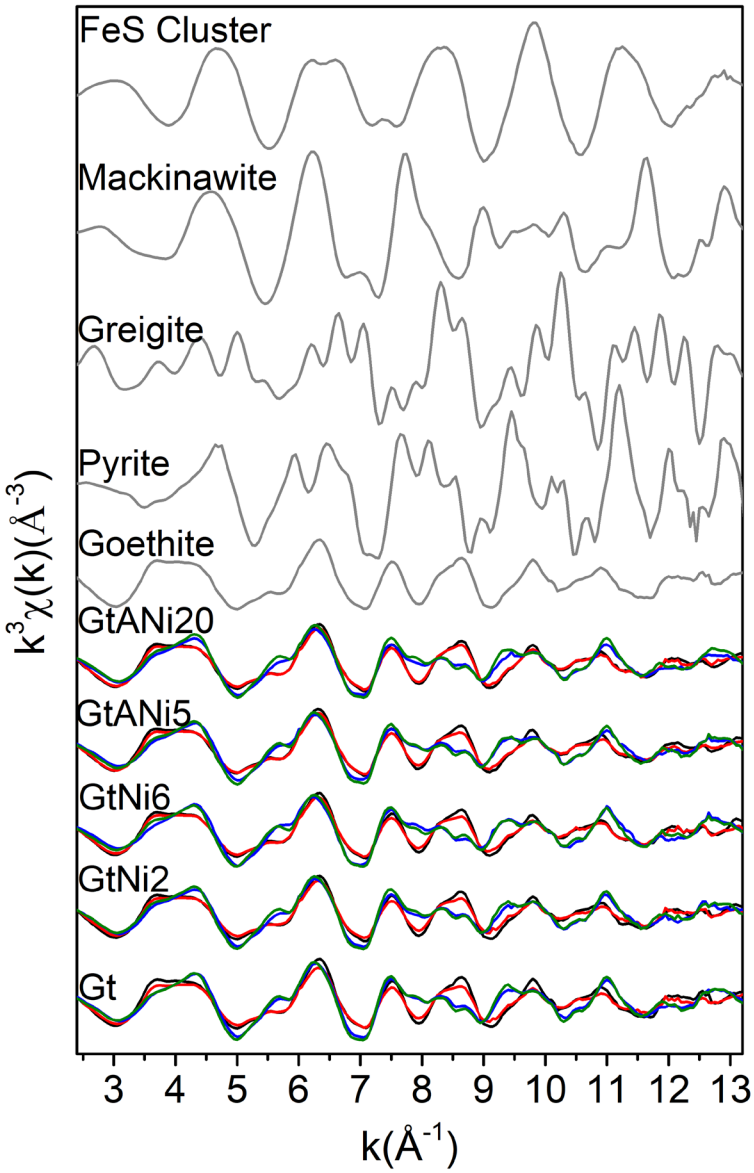

Fig. S2. Fe K-edge EXAFS spectra (k^3 weighted) obtained for pristine (black) and sulfidized goethite samples (red: 3 days, blue: 7 days, olive green: 44 days), and iron oxyhydroxide/sulfide standards (gray). Data for colloidal FeS from Noël et al. (2020). The Fe K-edge EXAFS spectrum of greigite was calculated with Feff8.4 (Ikogou et al., 2017) based on its structure model (COD#9000123).

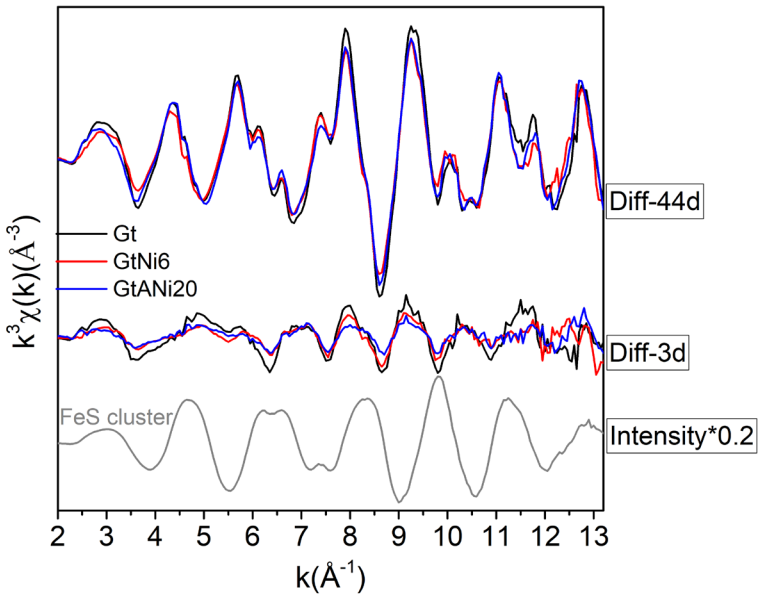

Fig. S3. Difference of Fe K-edge EXAFS spectra (k^3 weighted) between pristine and sulfidized samples (3 or 44 days of sulfidation) by comparison with a FeS cluster standard.

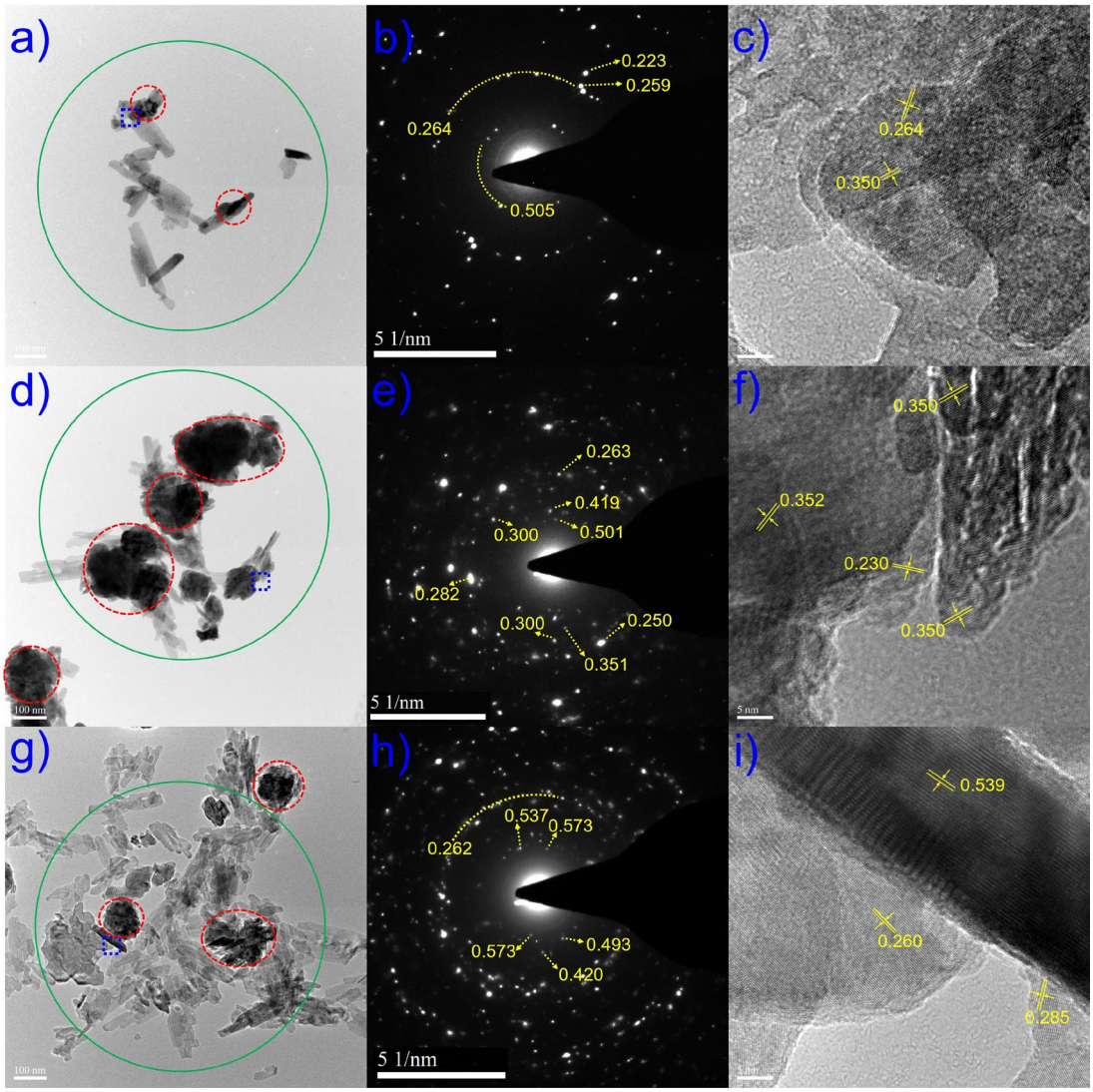

Fig. S4. Low magnification TEM images (scale bar is 100 nm) of samples sulfidized for 44 days: a): Gt-44d, d): GtNi6-44d, and g): GtANi20-44d. Those fibrous morphologies represent residual goethite crystals, and red dotted circles outlining polycrystalline aggregates indicate iron sulfides. b), e), and h): selected area electron diffraction (SAED) patterns of green circles indicated areas in a), d), and g), respectively. c), f), and i): high magnification images (scale bar is 5 nm) of the blue dotted rectangles shown in a), d), and g), respectively. Yellow values plotted on SAED patterns and lattice fringe images are distances (in *nm*). In particular, ~0.282/0.285, ~0.350, and 0.573 nm correspond to (222), (220), and (111) of greigite (ICDD#16-0713) respectively, and that of ~0.537/0.539 nm are ascribed to (100) of pyrite (ICDD#42-1340), and ~0.300 nm indicates (311) of greigite or (101) of mackinawite (ICDD#15-0037). These numbers above couldn't be attributed to any plane of goethite (ICDD#29-0713).

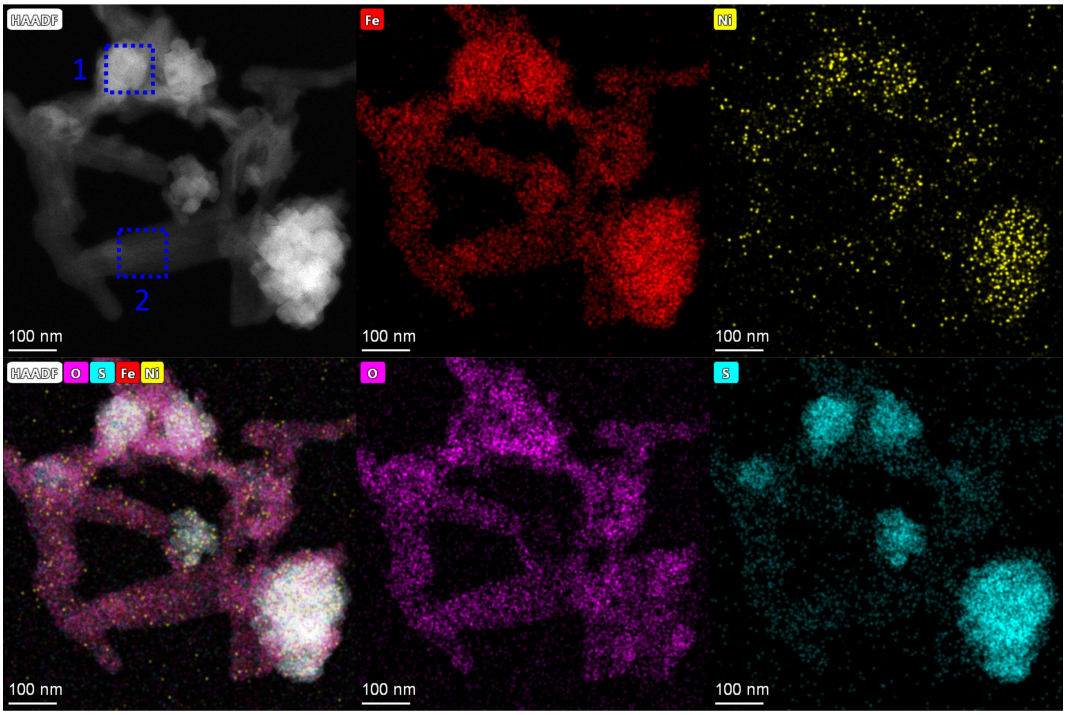

Fig. S5. STEM/HAADF micrograph (upper left) and EDX maps for Fe (upper center), Ni (upper right), O (lower center), S (lower right), and composite Fe-Ni-S-O obtained for GtNi6-44d. Ni mass fraction in area #1 (HAADF image) was 1.0±0.2%, that in area #2 was 0.8±0.5%.

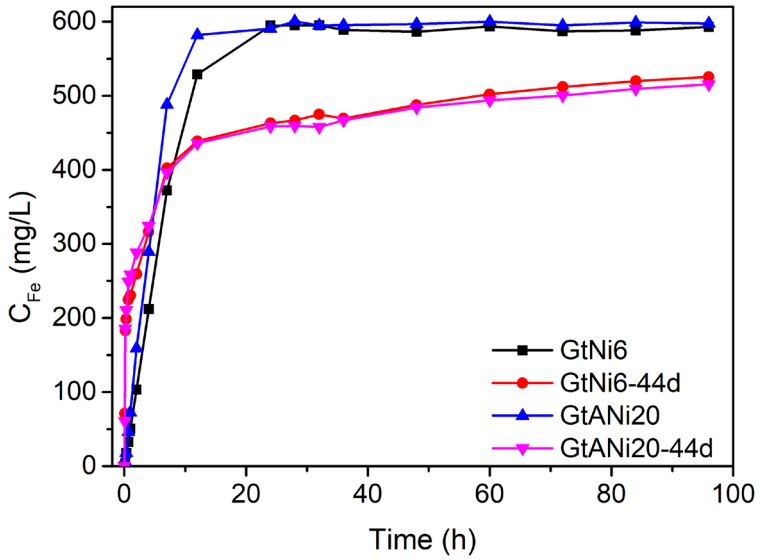

Fig. S6. Kinetic release of Fe (in concentration) during HCl treatment of pristine GtNi6 and GtANi20 and of their sulfidized counterparts. After 24 hrs, ~75% of Fe initially present in pristine goethites has been released from sulfidized samples.

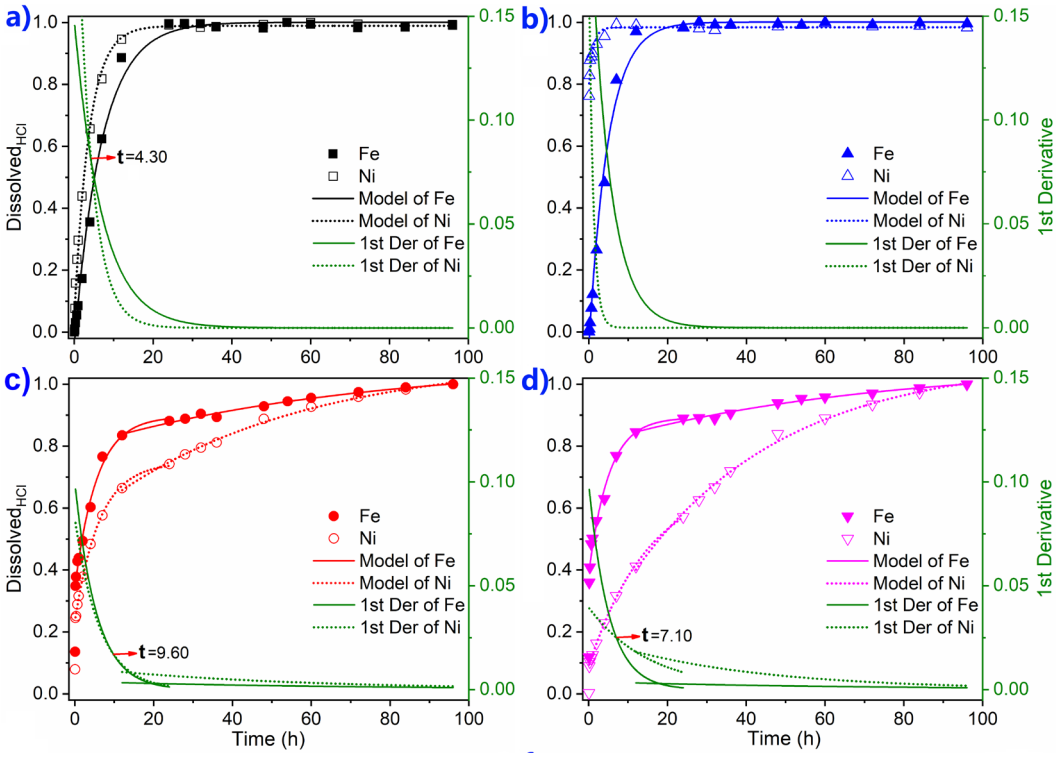

Fig. S7. Modeling of Fe and Ni kinetic release and corresponding 1st derivatives during HCl treatment of a) GtNi6, b) GtANi20, c) GtNi6-44d, and d) GtANi20-44d. Fits to the Fe and Ni data are shown as solid and dotted lines, respectively. 1st derivative curves are shown as green lines. Red arrows in a), c), and d) indicate the point where the 1st derivatives of Fe and Ni release are equal.

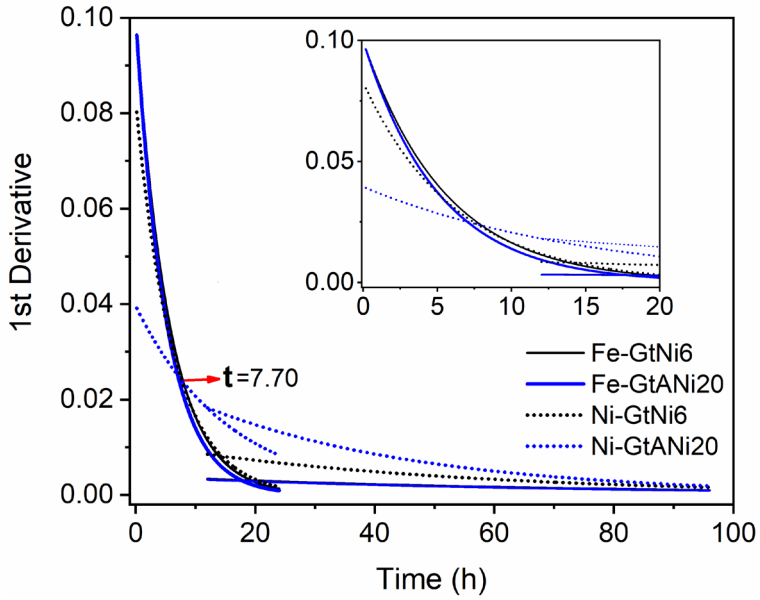

Fig. S8. First derivative of modeled Fe and Ni kinetic release of GtNi6 and GtANi20.

Table S1

Relative contents of Fe-bearing minerals determined from Rietveld refinement of XRD data in pristine Ni-free/-containing goethites and corresponding reaction products after interaction with S(-II).

Sample	Time	Goethite	Pyrite	Greigite	Mackinawite
		f%	f%/f_S%	f%/f_S%	f%/f_S%
Gt	0d	100	-/-	-/-	-/-
	3d	98.1	1.0(2)/-	0.1(1)/-	0.8(1)/-
	7d	61.7(5)	35.8(5)/93.7	0.6(2)/1.5	1.9(1)/4.8
	25d	59.5(5)	38.5(5)/95.1	1.1(2)/2.8	0.9(1)/2.1
	44d	41.5(5)	54.4(5)/92.8	2.8(2)/4.8	1.4(1)/2.4
GtNi2	0d	100	-/-	-/-	-/-
	3d	97.4	1.6(1)/-	0.2(1)/-	0.8(1)/-
	7d	70.9(5)	27.5(5)/94.6	0.4(1)/1.5	1.1(1)/3.9
	25d	57.8(6)	37.7(5)/89.4	3.3(2)/7.8	1.2(1)/2.8
	44d	54.1(5)	33.2(4)/72.4	9.7(3)/21.2	3.0(1)/6.5
GtNi6	0d	100	-/-	-/-	-/-
	3d	97.9	1.4(1)/-	-/-	0.7(1)/-
	7d	58.2(7)	39.1(6)/93.5	0.9(2)/2.2	1.8(1)/4.2
	25d	52.0(6)	33.9(5)/70.6	13.2(4)/27.4	1.0(1)/2.0
	44d	53.8(5)	33.5(5)/72.5	11.5(3)/24.8	1.3(1)/2.7
GtANi5	0d	100	-/-	-/-	-/-
	3d	97.8	1.6(1)/-	-/-	0.6(1)/-
	7d	66.0(6)	31.5(5)/92.5	0.8(2)/2.5	1.7(1)/5.0
	25d	57.3(6)	38.2(5)/89.5	3.0(2)/7.0	1.5(1)/3.6
	44d	50.4(6)	33.0(5)/66.6	11.0(3)/22.1	5.6(2)/11.2
GtANi20	0d	100	-/-	-/-	-/-
	3d	99.1	0.5(1)/-	0.3(1)/-	0.1(1)/-
	7d	69.1(5)	29.2(5)/94.6	0.4(2)/1.4	1.2(1)/4.0
	25d	48.5(8)	36.2(8)/70.3	13.9(8)/26.9	1.4(1)/2.8
	44d	47.6(5)	40.7(5)/77.7	3.7(2)/7.0	8.0(2)/15.3

Note: f% represents the mass fraction (wt.%) of a specific mineral in the samples, whereas f_S% represents the relative proportion of this mineral among iron sulfides (pyrite + greigite + mackinawite).

Table S2

Unit-cell parameters of Fe-bearing minerals in pristine Ni-free/-containing goethites and corresponding reaction products and fit quality parameters of the Rietveld refinement.

Sample	Time	Rwp	χ^2	Goethite			Pyrite	Greigite	Mackinawite	
				a	b	c	a	a	a	c
Gt	0d	2.05	1.27	4.629(5)	9.957(6)	3.025(2)	--	--	--	--
	3d	2.33	1.24	4.626(9)	9.958(10)	3.023(3)	5.435(12)	9.975	3.697(42)	5.083(66)
	7d	3.22	2.35	4.629(9)	9.964(12)	3.025(4)	5.427(5)	9.975	3.698(19)	5.083
	25d	3.75	1.42	4.630(12)	9.964(16)	3.025(5)	5.430(6)	9.922(47)	3.710	5.083
	44d	3.10	2.08	4.631(8)	9.963(11)	3.024(3)	5.429(4)	9.884(18)	3.662(23)	5.072(34)
GtNi2	0d	2.56	1.42	4.624(7)	9.966(8)	3.027(2)	--	--	--	--
	3d	2.49	1.21	4.619(8)	9.959(10)	3.022(3)	5.432(8)	9.953(28)	3.680(37)	5.083
	7d	3.00	1.98	4.620(10)	9.962(13)	3.023(4)	5.431(6	9.975	3.704(27)	5.083
	25d	3.50	1.90	4.628(10)	9.968(13)	3.024(4)	5.433(5)	9.890(19)	3.672(31)	5.078(46)
	44d	2.90	2.06	4.622(7)	9.961(9)	3.023(2)	5.429(3)	9.872(17)	3.668(7)	5.050(15)
GtNi6	0d	2.22	1.31	4.624(5)	9.967(6)	3.026(2)	--	--	--	--
	3d	2.47	1.37	4.624(7)	9.965(9)	3.024(3)	5.435(8)	--	3.710	5.083
	7d	3.33	2.10	4.625(13)	9.975(18)	3.026(5)	5.439(6)	9.975	3.685(21)	5.083
	25d	2.88	1.90	4.621(8)	9.966(11)	3.022(3)	5.433(4)	9.875(17)	3.692(22)	5.083
	44d	2.70	1.70	4.622(7)	9.967(10)	3.023(3)	5.433(3)	9.879(14)	3.660(17)	5.063(26)
GtANi5	0d	2.08	1.17	4.629(4)	9.956(5)	3.025(1)	--	--	--	--
	3d	2.27	1.20	4.624(7)	9.955(9)	3.023(3)	5.425(7)	--	3.710	5.083
	7d	3.15	2.07	4.625(9)	9.961(12)	3.024(3)	5.433(6)	9.975	3.695(23)	5.083
	25d	3.13	1.76	4.630(9)	9.967(14)	3.025(3)	5.435(5)	9.907(20)	3.666(23)	5.083
	44d	2.79	1.67	4.624(8)	9.962(10)	3.023(3)	5.432(4)	9.877(13)	3.670(5)	5.045(10)
GtANi20	0d	2.12	1.23	4.629(4)	9.956(5)	3.025(1)	--	--	--	--
	3d	2.13	1.11	4.626(7)	9.960(8)	3.025(2)	5.440(14)	9.783(110)	3.710	5.083
	7d	2.96	1.95	4.628(10)	9.968(13)	3.026(4)	5.439(6)	9.975	3.710	5.083
	25d	3.18	1.95	4.633(10)	9.965(15)	3.025(4)	5.438(5)	9.887(76)	3.683(23)	5.049(36)
	44d	3.15	1.84	4.624(8)	9.960(11)	3.023(3)	5.432(4)	9.883(14)	3.672(4)	5.047(10)

Table S3

Kinetic parameters computed for Fe (y_1) and Ni (y_2) release from solids in HCl solutions.

Acid Treatment	HCl	
Time	0.167-24 h	24-96 h
GtNi6	$y_1=-1.04*e^{-t/7.02}+1.00$, $r^2=0.9957$; $y_2=-0.94*e^{-t/3.75}+0.99$, $r^2=0.9970$;	
GtANi20	$y_1=-1.05*e^{-t/4.90}+1.00$, $r^2=0.9955$; $y_2=-0.20*e^{-t/1.09}+0.98$, $r^2=0.9346$;	
GtNi6-44d	$y_1=-0.55*e^{-t/5.55}+0.90$, $r^2=0.9932$; $y_2=-0.51*e^{-t/6.22}+0.75$, $r^2=0.9989$;	$y_1=-0.28*e^{-t/69.25}+1.07$, $r^2=0.9888$; $y_2=-0.55*e^{-t/45.94}+1.07$, $r^2=0.9903$;
GtANi20-44d	$y_1=-0.51*e^{-t/5.09}+0.89$, $r^2=0.9832$; $y_2=-0.61*e^{-t/15.41}+0.70$, $r^2=0.9993$;	$y_1=-0.26*e^{-t/67.69}+1.06$, $r^2=0.9956$; $y_2=-0.93*e^{-t/37.01}+1.07$, $r^2=0.9956$;

References:

Ikogou M., Ona-Nguema G., Juillot F., Le Pape P., Menguy N., Richeux N., Guigner J. M., Noel V., Brest J., Baptiste B. and Morin G. (2017) Long-term sequestration of nickel in mackinawite formed by Desulfovibrio capillatus upon Fe(III)-citrate reduction in the presence of thiosulfate. *Appl. Geochem.* **80**, 143-154.

Noël V., Kumar N., Boye K., Barragan L., Lezama-Pacheco J. S., Chu R., Tolic N., Brown G. E. and Bargar J. R. (2020) FeS colloids - formation and mobilization pathways in natural waters. *Environ. Sci. Nano* **7**, 2102-2116.